Extracellular Vesicles Deliver Mitochondria and HSP27 Protein to Protect the Blood-Brain Barrier

Kandarp M. Dave[1], Michael John Reynolds[2], Donna B. Stolz[3], Riyan Babidhan[1], Duncan X. Dobbins[1], Hannah Yankello[4], Rohan Reddy[1], Younsoo Bae[5], Sruti S. Shiva[2,6], Devika S Manickam[1]

[1]Graduate School of Pharmaceutical Sciences, Duquesne University, Pittsburgh, PA

[2]Pittsburgh Heart Lung Blood Vascular Institute, University of Pittsburgh Medical School, Pittsburgh, PA

[3]Center for Biologic Imaging, University of Pittsburgh Medical School, Pittsburgh, PA

[4]Departments of Chemical and Biomedical Engineering, Carnegie Mellon University, Pittsburgh, PA

[5]Department of Pharmaceutical Sciences, College of Pharmacy, The University of Kentucky, Lexington, KY

[6]Department of Pharmacology & Chemical Biology, University of Pittsburgh Medical School, Pittsburgh, PA

†Corresponding author:

Devika S Manickam, Ph.D.

600 Forbes Avenue, 453 Mellon Hall

Pittsburgh, PA 15282.

Email: soundaramanickd@duq.edu, Twitter: @manickam_lab

Phone: +1 (412) 396-4722, Fax +1 (412) 396-2501

Highlights

- Exosomes and microvesicles (EVs) can be engineered for co-delivery of bio-actives
- Microvesicles (MV) but not exosomes contain functional mitochondria
- MV mitochondria fused with the mitochondria in recipient brain endothelial cells
- MVs increase mitochondrial function while EVs increase cellular ATP levels
- EV-mediated HSP27 delivery decreased dextran permeability in brain endothelial cells

Abstract

Ischemic stroke causes brain endothelial cell death and damages tight junction integrity of the blood-brain barrier (BBB). We engineered endothelial cell-derived extracellular vesicles (EVs) for the delivery of exogenous heat shock protein 27 (HSP27) and harnessed the innate EV mitochondrial load as a one, two-punch strategy to increase brain endothelial cell survival (via mitochondrial delivery) and preserve their tight junction integrity (via HSP27 delivery). We demonstrated that endothelial microvesicles but not exosomes transferred their mitochondrial load that subsequently underwent fusion with the mitochondrial network of the recipient primary human brain endothelial cells. This mitochondrial transfer increased the relative ATP levels and mitochondrial function in the recipient endothelial cells. EV-mediated HSP27 delivery to primary human brain endothelial cells decreased the paracellular permeability of small and large molecular mass fluorescent tracers in an *in vitro* model of ischemia/reperfusion injury. This one, two-punch approach to increase the metabolic function and structural integrity of brain endothelial cells is a promising strategy for BBB protection and prevention of long-term neurological dysfunction post-ischemic stroke.

48 # Graphical Abstract

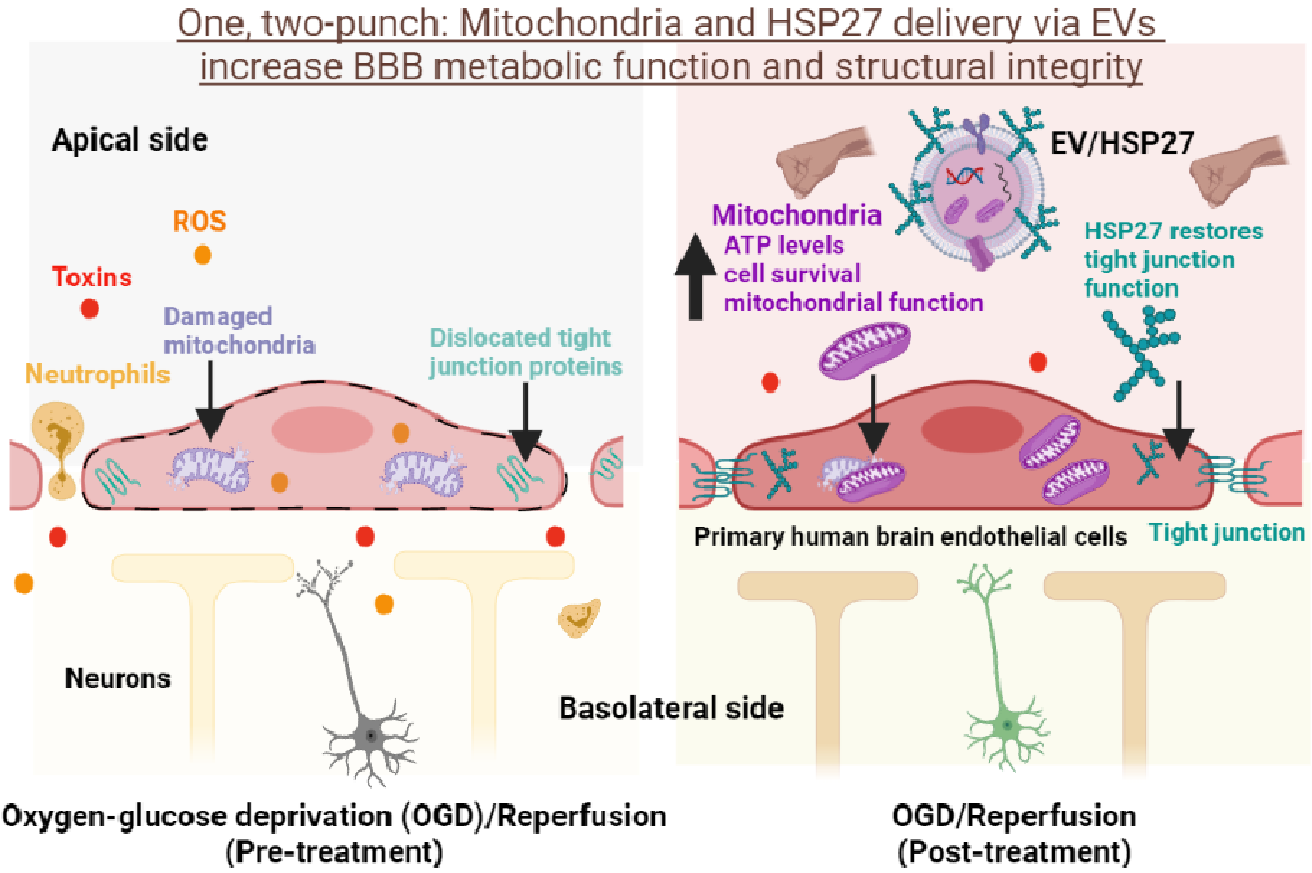

49

50

51

52 # Keywords

53 Extracellular vesicles, mitochondria, microvesicles, heat shock protein, paracellular

54 permeability, BBB

Abbreviations

ATP	Adenosine triphosphate
BBB	Blood-brain barrier
BECs	Brain endothelial cells
Calcein AM	Calcein acetoxymethyl
ECAR	Extracellular acidification rate
EVs	Extracellular vesicles (exosomes and microvesicles)
EXOs	Exosomes
FT cycle	Freeze/Thaw cycle
GAPDH	Glyceraldehyde 3-phosphate dehydrogenase
HSP27	Heat shock protein 27
hCMEC/D3	human cerebral microvascular endothelial cell line
HBMEC	primary human brain microvascular endothelial cells
HEPES	2-Hydroxyethylpiperazine-N'-2-Ethanesulfonic Acid
MVs	Microvesicles
MitoT-red-EV	Mitotracker deep red-labeled extracellular vesicles
OCR	Oxygen consumption rate
OGD	Oxygen-glucose deprivation
OGD/RP	Oxygen-glucose deprivation/reperfusion
PEI	Polyethylenimine
PEG-DET	poly (ethylene glycol)-*b*-poly (diethyl triamine)
ROS	Reactive oxygen species
TRITC	Tetramethyl rhodamine iso-thiocyanate

1. Introduction

Acute ischemic stroke is a major cause of death worldwide with recurrence and mortality rates of one stroke per 40 seconds and four deaths per minute, respectively, in the United States of America (1). During the onset of ischemic stroke, the blood flow to a brain artery is obstructed due to blood clots and plaque formation, which leads to long-term neurological damage and dysfunction or even death (2). The lack of blood supply to the affected brain area causes the deprivation of vital ions, oxygen, and nutrients consequently resulting in sudden cellular energy failure, neuron depolarization, reactive oxygen species-mediated cell death, and blood-brain barrier (BBB) dysfunction (2-4). Alteplase (recombinant tissue plasminogen activator) is the only FDA-approved treatment for ischemic stroke which dissolves the blood clot and restores the blood flow (5). However, its narrow therapeutic window (<4.5 h of onset) limits its use to only about 5% of patients (4). Importantly, the reestablishment of blood flow in the affected brain area outside its therapeutic window contributes to the influx of water and osmotic solutes through the damaged BBB (ischemia/reperfusion) and consequently, aggravates the BBB breakdown and risk of hemorrhagic transformation (4, 6). The limited therapeutic options and the associated severe side effects associated with Alteplase drive the development of safe and efficient stroke therapeutics.

Oxygen and glucose deprivation (OGD) in ischemic stroke reduce ATP levels in the endothelial cells lead to impaired functionality of Na^+-K^+-ATPase and Ca^{2+} ATPase activity which accumulates these cations within the cells (3, 4). This further leads to Na^+ and water influx that causes endothelial swelling and breakdown of the BBB. Na^+ accumulation-mediated depolarization of endothelial plasma membrane also rapidly increases intracellular Ca^{2+} and

activates the release of excitatory neurotransmitters such as glutamate and dopamine (7). Intracellular calcium overload catalyzes enzymatic activities leading to protein degradation, DNA damage, generation of reactive oxygen species (ROS), mitochondrial dysfunction, and the subsequent impairment of mitochondrial ROS defense mechanisms. Overall, hypoperfusion in the ischemic brain region leads to a rapid decrease in endothelial ATP levels, endothelial swelling, and mitochondrial dysfunction. Therefore, restoring the endothelial bioenergetics and mitochondrial function is a viable strategy to rescue ischemic endothelial cell death. In addition, disruption of the BBB is a major hallmark of ischemic stroke that is associated with altered expression of tight junctions, adherens junction proteins, and BBB transporters (2-4). Early ischemia/reperfusion activates the polymerization of the actin cytoskeleton in endothelial cells which triggers the formation of F-actin and myosin-containing contractile stress-fibers. These force-generating fibers transmit tension to the tight and adherens junction proteins which disassemble and internalize the tight junction proteins and consequently lead to the loss of barrier properties of the endothelial cells lining the BBB (8, 9). Uncontrolled actin polymerization-induced breakdown of BBB leads to infiltration of proinflammatory mediators, blood cells, circulatory immune cells, and toxins into the brain parenchyma, and lead to the secondary injury cascade (9, 10). Hence, a combined strategy to increase the endothelial cell bioenergetics to decrease cell death and reduce their paracellular permeability, ultimately leading to protection of BBB integrity is a viable approach for the treatment of ischemia/reperfusion injury.

Preclinical studies have demonstrated that endothelial, but not neuronal overexpression of heat shock protein 27 (HSP27), inhibited actin polymerization and elicited long-lasting protection against ischemia/reperfusion-induced BBB disruption and neurological deficits (9,

10). Lower endothelial HSP27 levels increase BBB permeability and slow down the recovery of the damaged BBB under pathological conditions (11). HSP27 binds to actin monomer and also sequesters globular-actin (G-actin) monomer in the endothelial cells that prevents the binding of G-actin to filamentous-actin (F-actin) and further inhibits tight junctional protein translocation in endothelial cells (9, 11-14). HSP27 (24-27 kD) is a highly conserved molecular chaperone from a small HSP family (15) and has multiple functionalities including suppression of caspase activation (16, 17), inhibition of cytochrome release (18), and reduction of protein aggregation. Intravenous administration of cell-penetrating transduction domain (TAT)-HSP27 rapidly enhanced HSP27 levels in brain microvessels and reduced infract volume as well as ischemia/reperfusion-induced BBB disruption (9). However, the systemic delivery of HSP27 using cationic TAT peptide resulted in non-specific uptake-associated side effects in the brain and other tissues (9). Therefore, the delivery of exogenous human recombinant HSP27 protein to the brain endothelial cells (BECs) using natural carriers like extracellular vesicles (EVs) can likely increase its specific uptake into BECs owing to inherent membrane affinity of BEC-derived EVs to parent/donor BECs (19, 20).

EVs (exosomes and microvesicles) are an emerging class of natural nanocarriers for biotherapeutics due to their known roles in intercellular communication, lower immunogenicity, and inherent homing capabilities to target cells (21, 22). Exosomes (EXOs) range from 30-200 nm in particle diameter and their biogenesis involves the inward budding of endosomal membranes that transforms into multivesicular bodies (MVBs) followed by their fusion with the plasma membrane and EXOs release into extracellular spaces (22). The biogenesis of microvesicles (MVs) involves their outward budding from the cell's plasma membrane with

particle diameters ranging from 100 – 1000 nm (22). The selective packaging of the functional mitochondria and mitochondrial proteins in the MVs can increase the bioenergetics of recipient cells by releasing their vesicular components, including mitochondria, nucleic acids, proteins, and lipids. Mitochondria play a central role in cellular energy production and regulation of cell death including apoptosis and autophagy (23). Ischemia-induced mitochondrial dysfunction initiates the generation of excessive reactive oxygen species, reduction in ATP levels, and consequently cellular and neuronal death (23). Therefore, protection of mitochondrial function via exogenous functional mitochondria supplementation is an exciting strategy to increase endothelial cell survival post-ischemic stroke. Thus, we rationalize that mitochondria-rich MVs derived from brain endothelial cells can increase cellular bioenergetics and survival under normoxic and hypoxic conditions.

Surface engineering of BEC-derived EVs with exogenous HSP27 is a promising strategy that can allow harnessing the inherent targeting capabilities of the EVs to the recipient BECs along with the added benefits of their mitochondrial load. Alongside BEC-derived EVs, we have also tested the capability of a synthetic cationic polymer, poly (ethylene glycol)-*b*-poly (diethyltriamine) (PEG-DET) to formulate and deliver HSP27. We have previously used PEG-DET polymer to form nanosized complexes with superoxide dismutase protein and demonstrated a >50% reduction in brain infract volume in a mouse model of acute ischemic stroke (24). PEG-DET is a cationic diblock copolymer known for its safety and gene transfer efficacy in comparison to commercial transfection agents such as lipofectamine, polyethyleneimine, and other cationic polymers (25-27).

Here, we *hypothesize* that the engineering of innate mitochondria-containing BEC-derived EVs with exogenous HSP27 protein is one double-punch approach to increase BEC survival (via mitochondrial delivery) and preserve its tight junction barrier via decreasing the paracellular permeability (via HSP27 delivery) of the endothelial monolayers post-ischemia. This approach will protect and strengthen the BBB that in turn can ameliorate the long-term neurological damage and dysfunction.

In this study, we isolated EXOs and MVs from hCMEC/D3: a human brain endothelial cell line using a sequential ultracentrifugation method (28) and characterized their particle diameter, zeta potential, and membrane integrity post-cold storage. While we collectively refer to both large (MV) and small (EXO) vesicle fractions as EVs, we have studied the singular effects of both MVs and EXOs. We demonstrated the presence of mitochondria in MV sections using transmission electron microscopy. We evaluated the effects of EV dose and incubation times on mitochondrial transfer to the recipient cells and demonstrated the integration of MV-delivered mitochondria with the mitochondrial network of the recipient endothelial cells. We studied the effects of EV exposure on the resulting relative ATP levels, mitochondrial respiration, and glycolytic capacity of the recipient endothelial cells under normoxic and hypoxic conditions. The formation of EV/HSP27 and PEG-DET/HSP27 complexes/mixtures and their physicochemical characteristics were confirmed using native polyacrylamide gel electrophoresis and dynamic light scattering. The cytocompatibility of EV/HSP27 mixtures and PEG-DET/HSP27 complexes were evaluated using an ATP assay. The effects of HSP27 delivery on the paracellular permeability of small and large molecule fluorescent tracers were evaluated under ischemic and ischemia/reperfusion conditions in primary human brain endothelial cultures.

2. Materials

Recombinant human HSP27 was purchased from Novus Biologicals (Centennial, CO). Cell Titer Glo 2.0 reagent (ATP assay) was procured from Promega (Madison, WI). Micro BCA and Pierce BCA protein assay kits were purchased from Thermo Scientific (Rockford, IL). PEG-DET polymer was synthesized by aminolysis of PEG-poly(β-benzyl L-aspartate) block copolymers with diethyltriamine as previously reported (25, 27, 29, 30). Bio-Safe Coomassie G-250 stain was purchased from Bio-Rad Laboratories Inc. (Hercules, CA). Collagen Type I was purchased from Corning (Discovery Labware Inc, Bedford, MA) and endothelial cell basal medium-2 (EBM-2) was procured from Lonza (Walkersville, MD). Hydrocortisone, human basic fibroblast growth factor and ascorbic acid were purchased from Sigma-Aldrich (Saint Louis, MO). Penicillin-Streptomycin solution and Chemically Defined Lipid Concentrate were procured from Invitrogen (Carlsbad, CA). Heat-inactivated fetal bovine serum was bought from Hyclone Laboratories (Logan, UT). Polycarbonate centrifuge tubes were purchased from Beckman Coulter, Inc. (Brea, CA). Electrophoresis sample buffer was purchased from Bio-Rad (Hercules, CA). RIPA buffer was procured from Alfa Aesar (Ward Hill, MA). PET track-etched membrane Falcon Cell Culture inserts of 0.4 µm pore size were procured from Corning (Discovery Labware Inc, Bedford, MA). TRITC 65-85 kD and 4.4 kD dextran was procured from Sigma (St. Louis, MO). A low-volume disposable cuvette (Part no. ZEN0040, Malvern) was used for particle size measurements. CellLight Mitochondria-GFP Backman 2.0 reagent, MitoTracker Green FM, and MitoTracker Deep Red FM, Dynabeads Protein G (cat#10003D), and DynaMag-2 magnetic stand (cat#12321D) were procured from Invitrogen (Eugene, OR). Mouse monoclonal antibodies against ATP5A, GAPDH, HSP27 were purchased from Abcam. Mouse monoclonal antibody

against CD9 was received from Life Technologies corporation (Eugene, OR), whereas Alexa Fluor 790-conjugated donkey anti-mouse IgG was received from Jackson ImmunoResearch Lab Inc (West Grove, PA).

2.1. Cell models

A human cerebral microvascular endothelial cell line (hCMEC/D3, catalog number. 102114.3C) was received from Cedarlane Laboratories (Burlington, Ontario) at passage number (P) 25, and cells between P25 and P35 were used in all experiments (19, 28). hCMEC/D3 cells were grown in tissue culture flasks, multiwell plates, or transwell inserts pre-coated using 0.15 mg/mL rat collagen I in a humidified 5% CO_2 incubator at 37 ± 0.5˚C (Isotemp, Thermo Fisher Scientific). The cells were cultured in complete growth medium composed of endothelial cell basal medium (EBM-2) supplemented with fetal bovine serum (5% FBS), penicillin (100 units/mL)-streptomycin (100 µg/mL) mixture, hydrocortisone (1.4 µM), ascorbic acid (5 µg/mL), Chemically Defined Lipid Concentrate (0.01%), 10 mM HEPES (pH 7.4), and bFGF (1 ng/mL). The complete growth medium was replenished every other day until the cells formed confluent monolayers. Prior to passage, the cells were washed using 1x phosphate buffer saline (PBS) and detached from the flask using 1x TrypLE Express Enzyme (gibco, Denmark). We received primary human brain microvascular endothelial cells (HBMEC, catalog no. ACBRI 376) from Cell Systems (Manassas, VA) at P3, and cells below P11 were used in all experiments. HBMECs maintained in Cell Systems Classic Culture Medium containing 1% culture boost were cultured in tissue culture flasks, multiwell plates, or transwell inserts pre-treated with attachment factors. The complete growth medium was replenished every day until the cells formed confluent monolayers. For passage, HBMEC monolayers were washed with

Passage Reagent Group 1 (PRG 1, dPBS/EDTA solution), detached with PRG 2 (dPBS/trypsin-EDTA solution) and PRG 3 (trypsin inhibitor solution).

2.2. Isolation of exosomes and microvesicles from hCMEC/D3 cells

It should be noted that while we collectively refer to both large (microvesicle: MV) and small (exosome: EXO) vesicle fractions as EVs, we study both MVs and EXOs. Wherever noted, a 1:1 w/w mixture of EXOs and MVs is collectively referred to as EVs. EXOs and MVs were isolated from conditioned medium supernatants of hCMEC/D3 cells using the differential ultracentrifugation method (28). Briefly, tissue culture flasks with 175 cm^2 growth area (T175) containing confluent hCMEC/D3 were washed with pre-warmed 1x PBS and incubated with serum-free medium for 48 h in a humidified 5% CO_2 incubator at 37 ± 0.5˚C. Post-incubation, the EV-conditioned medium was collected in polypropylene centrifuge tubes and centrifuged at 2000 ×g for 22 min at 4°C to pellet down apoptotic bodies and cell debris using a Sorvall ST 8R centrifuge (ThermoFisher Scientific, Osterode am Harz, Germany). The supernatant was transferred into polycarbonate tubes and centrifuged at 20,000 ×g for 45 min at 4°C to pellet down MVs using an Optima XE-90 ultracentrifuge equipped with a 50.2 Ti rotor (Beckman Coulter, Indianapolis, IN). Next, the supernatant was filtered through a 0.22 µm PES membrane syringe filter, and the flow-through was centrifuged at 120,000 ×g for 70 min at 4°C to collect EXOs. Lastly, MV and EXO pellets were washed with 1x PBS and suspended in either 1x PBS for particle diameter measurements and *in vitro* experiments or 10 mM HEPES buffer pH 7.4 for zeta potential measurements. EXO and MV samples were stored at -80°C until further use. The total protein content in EXOs and MVs was quantified using Pierce MicroBCA assay. Briefly, EXOs and MVs were lysed with 1x RIPA buffer containing 3 µg/mL aprotinin at a 1:15 v/v

ratio. Following that, a 150 µL volume of EXO/MV lysates or BSA standards (0.5–200 µg/mL) was pipetted into a 96-well plate and an equal volume of the MicroBCA working reagent (reagent A: reagent B: reagent C at 25:24:1 volume ratio) was added to each well. The reagent mixture was incubated at 37 °C for 2 h and the absorbance was measured at 562 nm using a SYNERGY HTX multi-mode reader (BioTek Instruments Inc., Winooski, VT).

2.3. Dynamic light scattering (DLS) and Nanoparticle tracking analysis (NTA)

The stability of naïve EVs under storage conditions was determined by their measuring particle diameter and zeta potential using dynamic light scattering. EV samples at 0.5 mg protein/mL in 1x PBS were frozen at -20°C for 24 h and thawed at room temperature for 30 min. Post-thawing, the particle diameters, and dispersity indices were measured using Malvern Zetasizer Pro (Worcestershire, UK). The freeze-thaw (FT) cycle was repeated three times and all samples were run in triplicate. Average particle diameter, dispersity index, and zeta potential values were reported as mean ± standard deviation. For NTA, stock samples of EXOs and MVs were diluted 100 times in PBS and analyzed on a multiple-laser ZetaView f-NTA Nanoparticle Tracking Analyzer (Particle Metrix Inc., Mebane, NC). Three 60 s videos were acquired at 520 nm laser wavelength for particle diameter and concentration measurements. Average particle diameter and concentration were reported as mean ± standard deviation.

2.4. Membrane integrity of EVs after isolation and upon storage conditions

The membrane integrity of EXOs and MVs post-isolation and upon revival after their storage conditions (described earlier in the DLS section) was determined using a calcein AM flow cytometry assay. First, polystyrene sub-micron-sized beads ranging from 0.2 – 2 µm particle

diameters were used to calibrate the Attune NxT flow cytometer. The calibration beads, EXO, and MV samples were tested and events captured in forward scatter (FSC) and side scatter (SSC) plots were analyzed using a small particle side scatter 488/10-nm filter (BL1) channel. EXOs and MVs were diluted to 20 µg protein/mL in PBS and incubated/stained with 10 µM calcein AM for 20 min at room temperature in the dark. Unstained EXOs and MVs were used to gate the background signals, whereas samples treated with 2% v/v Triton X-100 followed by staining with calcein AM were used as controls to determine if calcein-positive signals were specifically associated with intact EVs. For each sample analysis, an aliquot of 100 µL was run through Attune NxT Acoustic cytometer (Invitrogen, Singapore) and 50,000 events were recorded during the run. The calcein-associated fluorescence intensity was detected at 488/10 nm and percentage signal intensities were presented in histogram plots generated using Attune software. Calcein AM-associated background signals were gated using the controls such as PBS containing 10 µM calcein AM and PBS/2% Triton X-100/calcein AM mixture.

2.5. Transmission Electron Microscopy analysis of EVs

Exosomes/microvesicles were loaded on Formvar/carbon-coated grids, negatively stained with 1% uranyl acetate and examined with a JEM-1400 Plus transmission electron microscope (JEOL, Peabody, MA, USA) fitted with an AMT digital camera (Danvers, MA, USA) (31). Suspensions of exosomes/microvesicles were pelleted at 100,000xg in a Beckman airfuge for 20 min and the pellets were fixed in 2.5% glutaraldehyde in PBS overnight. The supernatant was removed and the cell pellets were washed 3x in PBS and post-fixed in 1% OsO_4, 1% $K_3Fe(CN)_6$ for 1 hour. Following 3 additional PBS washes, the pellet was dehydrated through a graded series of 30-100% ethanol. After several changes of 100% resin over 24 hours, pellet was

embedded in a final change of resin, cured at 37^{o}C overnight, followed by additional hardening at 65^{o}C for two more days. Ultrathin (70 nm) sections were collected on 200 mesh copper grids, stained with 2% uranyl acetate in 50% methanol for 10 minutes, followed by 1% lead citrate for 7 min. Sections were imaged using a JEOL JEM 1400 Plus transmission electron microscope (Peabody, MA) at 80 kV fitted with a side mount AMT 2k digital camera (Advanced Microscopy Techniques, Danvers, MA).

2.6. Uptake of Mitotracker-labeled EVs into hCMEC/D3 cells using flow cytometry

2.6.1. Isolation of mitochondria-labeled EVs

hCMEC/D3 cells (P32) were cultured in a T175 flask to confluency. The complete growth medium was removed, cells were washed with 1x PBS, and cells were incubated with 250 nM Mitotracker deep red (MitoT-red) diluted in a conditioned medium for 30 min in a humidified incubator. Next, the medium was replaced with serum-free medium after washing the cells with 1x PBS, and cells were kept in a humidified incubator for 24 h. Post-incubation, the conditioned medium was collected into centrifuge tubes. EXOs (MitoT-red-EXO) and MVs (MitoT-red-MV) from Mitotracker Red-labeled cells were isolated from the conditioned medium using the differential centrifugation method described in section 2.2. The EV protein content in MitoT-red-EXOs and MitoT-red-MVs were determined using MicroBCA assay and the samples were stored at -80 °C until further use.

2.6.2. Quantification of EV-mediated mitochondria transfer into recipient hCMEC/D3 cells using flow cytometry

hCMEC/D3 cells were cultured in 48-well plates at 50,000 cells/well in complete growth medium. Unstained and untreated cells were used as a control, whereas cells stained with 250 nM of Mitotracker deep red (MitoT-red) for 45 min in complete growth medium were used as a positive control. The cells were treated with MitoT-red-EXOs and MitoT-red-MVs at 30, 75, and 150 µg EV protein/well in complete growth medium for 72 h in a humidified incubator. The cells were also treated with unlabeled EXOs and MVs at 150 µg EV protein/well in complete growth medium for 72 h. Post-treatment, the cells were washed with 1x PBS, dissociated using TrypLE Express, diluted with PBS, and collected into centrifuge tubes. For each sample, an aliquot of a 100 µL cell suspension was analyzed through Attune NxT Flow cytometer and 10,000 events were recorded in FSC vs. SSC plots. The Mitotracker deep red-associated fluorescence intensity was detected at 670/14 nm and percentage signal intensities were presented in histogram plots generated using Attune software version 3.2.3. Mitotracker deep red-associated background signals were gated using the controls including PBS and untreated cells.

2.7. Uptake of Mitotracker-labeled EVs into primary human brain endothelial cells using fluorescence microscopy

2.7.1. Uptake of MitoT-red-EXOs and MitoT-red-MVs into primary HBMEC monolayers

MitoT-red EXOs and MitoT-red-MVs were isolated from the conditioned medium of hCMEC/D3 cells as described in section 2.6.1. Primary HBMEC (P6) were cultured in 96-well plates at 16,500 cells/well in complete growth medium. Post-confluency, the cells were treated with MitoT-red-EXO and MitoT-red-MV at 10, 25, and 50 µg EV protein/well in complete growth medium for 24, 48, and 72 h in a humidified incubator. At each time-point, the cells were observed under an Olympus IX 73 epifluorescent inverted microscope (Olympus, Pittsburgh,

PA) using the Cyanine-5 (Cy5, excitation 651 nm, and emission 670 nm) and bright-field channels at 20x magnification. Images were acquired using CellSens Dimension software (Olympus, USA).

2.7.2. Colocalization of EV-mitochondria with the mitochondrial network in the recipient hCMEC/D3 and HBMEC monolayers

2.7.2.1. Mitotracker green staining of recipient cell mitochondria

HBMEC and hCMEC/D3 cells were seeded in a 96 well-plate at 16,500 cells/well and incubated in a humidified incubator at 37°C. Post-confluency, the complete growth medium was removed, cells were washed with 1x PBS, and cells were incubated with 250 µM of Mitotracker green in a complete medium for 30 min. Post-treatment, the medium was replaced, washed with PBS, and incubated with MitoT-red-EXO or MitoT-red-MV at 50 µg EV protein/well in a complete growth medium for 72 h in a humidified incubator. hCMEC/D3 cells stained with only Mitotracker green were used as a control. Post-incubation, the medium was removed, cells were washed and incubated with phenol-red free and serum-containing DMEM-high glucose medium. The cells were then observed under an Olympus IX 73 epifluorescent inverted microscope (Olympus, Pittsburgh, PA) using Cyanine-5 channel (Cy5, excitation 651 nm, and emission 670 nm) to detect MitoT-red-EV uptake and GFP channel to detect Mitotracker Green signals at 20x magnification and images were acquired using CellSens Dimension software (Olympus, USA).

2.7.2.2. Staining of a mitochondrial matrix protein in the recipient cells using CellLight Mitochondria-GFP BackMam reagent

We used CellLight Mitochondria-GFP BacMam to label a structural mitochondrial matrix protein (32). CellLight Mito-GFP is a fusion construct of the leader sequence of a mitochondrial matrix protein, E1 alpha pyruvate dehydrogenase, and emerald Green Fluorescent Protein (emGFP). HBMEC and hCMEC/D3 cells were seeded in a 96 well-plate at 16,500 cells/well and incubated in a humidified incubator at 37°C. Post-confluency, the complete growth medium was removed, cells were washed with 1x PBS, and cells were incubated with CellLight Mitochondria-GFP reagent (at a dilution of 2 µL/10,000 cells as recommended by the manufacturer) for 16 h. Post-transduction, the medium was removed and cells were washed with 1x PBS. Next, the cells were incubated with MitoT-red-EXO and MitoT-red-MV at 50 µg EV protein/well in complete growth medium for 72 h in a humidified incubator. HBMEC or hCMEC/D3 cells transduced with only CellLight Mitochondria-GFP were used as a control. Post-incubation at 24 and 72 h, the medium was removed, cells were washed and incubated with phenol-red free and serum-containing DMEM-high glucose medium. The cells were then observed under Olympus IX 73 epifluorescent inverted microscope (Olympus, Pittsburgh, PA) using Cyanine-5 channel (Cy5, excitation 651 nm, and emission 670 nm) to detect MitoT-EV uptake and GFP channel for CellLight Mitochondria-GFP signals at 20x magnification and images were acquired using CellSens Dimension software (Olympus, USA).

2.8. Effects of naïve EV treatment in primary HBMECs under normoxic and oxygen-glucose-deprived (OGD) conditions

To simulate ischemic conditions *in vitro,* hCMEC/D3 cells were exposed to different oxygen glucose-deprivation (OGD) parameters, and the resulting cell viability was evaluated using an ATP assay (28, 33, 34). hCMEC/D3 cells were cultured in 96-well plates at 16,500 cells/well.

Confluent hCMEC/D3 cells were incubated with OGD medium defined as follows: 120 mM NaCl, 5.4 mM KCl, 1.8 mM $CaCl_2$, 0.8 mM $MgCl_2$, 25 mM Tris-HCl, pH 7.4 for 0.5 to 24 h in either normoxic or hypoxic conditions (35). For normoxic conditions, the culture plates were incubated in a humidified incubator with 95% air and 5% carbon dioxide whereas for hypoxic conditions, the culture plates were incubated in an OGD chamber (Billups Rothenberg, Del Mar, CA) pre-flushed with 5% carbon dioxide, 5% hydrogen and 90% nitrogen at 37±0.5˚C. For normoxic conditions, the medium was removed and the recipient HBMEC monolayers were incubated with hCMEC/D3-derived EXOs, MVs, and EXOs+MVs at doses of 10, 25, and 50 µg EV protein/well in a humidified incubator for 24, 48, and 72 h. For hypoxic conditions, the medium was removed and the recipient HBMEC monolayers were incubated with hCMEC/D3-derived EXOs, MVs, and EXOs+MVs at doses of 10, 25, and 50 µg EV protein/well in the OGD medium and a humidified incubator for 24 h. Then, the treatment mixtures were replaced with pre-warmed complete growth medium, and an equal quantity of Cell Titer Glo 2.0 reagent was added. The plates were incubated for 15 min at RT on an orbital shaker in the dark and relative luminescence units were measured at 1 s integration time.

2.9. Measurement of mitochondrial function using Seahorse Analysis

The oxidative phosphorylation and glycolytic functions of hCMEC/D3 cells treated with EVs during normoxic conditions were evaluated using the Seahorse analysis by measuring oxygen consumption rate (OCR) and Extracellular Acidification rate (ECAR) (19, 36). hCMEC/D3 cells seeded at 20,000 cells/well were cultured in Seahorse XF96 plate for four days. The cells were incubated with hCMEC/D3-derived EXOs, MVs, and EXOs+MVs for 24, 48, and 72h at 3.4, 8.3, and 16.5 µg EV protein/well equivalent to 30, 75, and 150 µg EV protein/cm^2 in complete

growth medium. Post-incubation, the medium was replaced with pre-warmed DMEM and subjected to Seahorse analysis (19). After measurement of baseline OCR, 2.5 µmol/L oligomycin A and 0.7 µmol/L carbonyl cyanide-p-trifluoromethoxyphenyl-hydrazone were consecutively added to measure the proton leak and maximal OCR, respectively (36). The total protein of the cells in each well was measured using Pierce BCA assay.

2.10. Complexation of HSP27 with PEG-DET, EXO, MV, and PEG-DET-EV

PEG-DET/HSP27 complexes were prepared using a rapid mixing method. A PEG-DET polymer solution prepared in 10 mM HEPES buffer, pH 7.4 was mixed with 2 µg HSP27 at PEG-DET/HSP27 w/w ratio 0.05, 0.2, 1, 5, 10, and 20:1 for 30 s. The mixture was incubated at room temperature (RT) for 30 min. For the preparation of EXO/HSP27 and MV/HSP27 mixtures, hCMEC/D3-derived EVs were suspended in 1x PBS were incubated with 2 µg HSP27 at EV protein/HSP27 w/w ratios 5, 10, and 15:1 in centrifuge tubes. The mixture was vortexed for 30 s and incubated at room temperature for 30 min. To prepare (PEG-DET/HSP27)/EV complexes, PEG-DET/HSP27 complexes were prepared at 20:1 and 30:1 w/w ratios followed by incubation with 10 µg EV protein for 30 min at RT. The different complexes were characterized for electrophoretic mobility, particle diameter, and zeta potential.

2.11. Native Polyacrylamide Gel Electrophoresis (PAGE)

The complexation of HSP27 with PEG-DET, EXO, and MV was confirmed using native PAGE. A polyacrylamide gel consisting of 4% and 10% of acrylamide in the stacking and resolving sections, respectively, was prepared using a gel casting assembly (Bio-Rad Laboratories Inc., Hercules, CA) (28, 33). Native HSP27, PEG-DET/HSP27, and EV/HSP27

complexes containing 2 µg of HSP27 at the indicated w/w ratios were mixed with native sample buffer and loaded into the gel lanes. Free PEG-DET polymer, naïve EXOs, and MVs equivalent to indicated w/w ratios were used as controls. In an independent experiment, PEG-DET/HSP27 at w/w 20:1 and 30:1 was complexed with EXOs, MVs, and EVs (EXO: MV 1:1) at PEG-DET to EV protein 2:1 and 3:1 w/w ratios. The gel was run in 1x Tris-Glycine buffer, pH 8.3 at 100 V for 2 h at 2-8 °C using PowerPac Basic setup (Bio-Rad Laboratories Inc., Hercules, CA). Post-electrophoresis, the gel was washed with deionized water for 30 min and stained with 50 mL of Biosafe Coomassie blue G-250 for 1 h on an orbital shaker at room temperature. The gel was washed with deionized water for 30 min and scanned under Odyssey imager (LI-COR Inc., Lincoln, NE) at 800 nm channel and intensity setting 5. The band densities were quantified using ImageStudio 5.2 software.

2.12. Dynamic light scattering analysis of HSP27 complexes

The average particle diameters, dispersity indices, and zeta potentials of the HSP27 complexes were analyzed using a Malvern Zetasizer Pro (Worcestershire, UK). hCMEC/D3 cell line-derived naïve EVs at 0.5 mg EV protein/mL were diluted in either 1x PBS for size and dispersity index or 10 mM HEPES buffer pH 7.4 for zeta potential measurements. In addition, particle sizes and dispersity indices of native HSP27 protein at 20 µg/mL, PEG-DET/HSP27 complexes at 10, 20, and 30:1 w/w ratios, EXO/HSP27 and MV/HSP27 mixtures at 10:1 w/w ratio were measured in a low-volume disposable cuvette. Free PEG-DET equivalent to 10, 20, and 30:1 w/w ratios and naïve EVs equivalent to 10:1 w/w ratio were also analyzed. For the zeta potential of the above complexes, a 50 µL sample of complexes was further diluted in zeta cuvette containing 10 mM HEPES buffer at pH 7.4. The samples were run in triplicate. Data are

467 presented as average particle diameter±standard deviation. The reported data are representative
468 of 3 independent experiments.
469
470 **2.13. Cytocompatibility of HSP27 complexes with primary HBMEC and hCMEC/D3**
471 **monolayers**
472 The cell viability of hCMEC/D3 and primary HBMEC monolayers treated with HSP27
473 complexes was measured using Cell Titer Glo (ATP) assay. hCMEC/D3 and HBMEC were
474 seeded at 16,500 cells/well in a 96 well-plate and cultured in a humidified incubator at 37±0.5˚C.
475 The growth medium was replaced with treatment mixtures containing either native HSP27,
476 EXO/HSP27 (10:1), MV/HSP27 (10:1), EXO+MV at 1:1/HSP27 (10:1), or PEG-DET/HSP27
477 (20:1) at a dose of 2 µg HSP27 protein per well. Naïve EXOs, MVs, equivalent amounts of
478 EXOs+MVs, and free PEG-DET equivalent to 20:1 in complete medium were used as controls.
479 Polyethyleneimine (PEI) at 50 and 100 µg/mL in a complete growth medium was used as a
480 positive control. The complexes and controls were treated for 72 h in a humidified incubator at
481 37±0.5˚C. Post-incubation, the ATP assay was performed using Cell Titer Glo 2.0 reagent as
482 described earlier in section 2.8. The cell viability of HSP27 complexes treated HBMECs was
483 calculated using Equation 1.

484 $$Cell\ viability\ (\%) = \frac{Relative\ light\ units\ (RLU) of\ treated\ cells}{RLU\ of\ untreated\ cells} \times 100 \qquad \text{(Equation 1)}$$

485
486 **2.14. Paracellular permeability of TRITC-labeled 65-85 and 4.4 kD Dextran in HBMEC**
487 **monolayers pre-treated with PEG-DET/HSP27 complexes**
488 **2.14.1 Hypoxic conditions (OGD only)**

Primary HBMEC (P4-P9) in a complete growth medium were seeded at 50,000 cells/cm^2 in a 24-well format cell culture insert (insert area: 0.33 cm^2) for four days to form a complete endothelial monolayer. The medium was replaced every 48 h during this culturing period. The abluminal wells were filled with complete growth medium throughout the culturing period. The complete growth medium was replaced with 300 µL of growth medium containing PEG-DET/HSP27 at a w/w ratio of 20:1 and a dose of 2 µg HSP27/well for 72 h. Post-treatment, the complete growth medium was replaced with 300 µL of OGD medium containing 1 µM TRITC-Dextran. The OGD medium containing 1µM TRITC-Dextran alone was used as a control. The medium containing 1µM TRITC-Dextran in complete growth medium alone was used as an additional control. The abluminal chamber was filled with 0.5 mL of fresh complete growth medium. The untreated group was incubated in a humidified incubator whereas OGD treatment groups were incubated in an OGD chamber (as described earlier in section 2.8.). The concentration of TRITC-Dextran in the abluminal medium was measured at 4, 6, and 24 h post-treatment. A 50 µL aliquot was collected at indicated time points from the abluminal side. An equal volume of fresh medium was replaced to maintain the sink conditions. The concentration of TRITC-Dextran was measured using Synergy HTX multimode plate reader at excitation 485/20 and emission 580/50 nm. The diffusion rate of TRITC-Dextran at each time point was calculated by the amount of TRITC- Dextran per surface area (0.33 cm^2) of the insert per time (30 min).

2.14.2. OGD/reperfusion

Post-24 h of OGD exposure, HBMECs in the culture inserts were washed with 1x PBS. HBMECs were incubated with a complete growth medium containing 1 µM TRITC 65-85 or 4.4

kD Dextran in a 24-well format cell culture insert for 1h – 24h (reperfusion) in a humidified incubator. The abluminal chamber was filled with 0.5 mL of fresh complete growth medium. The concentration of TRITC-Dextran in the abluminal medium was measured at 1, 2, and 4, and 24 h during reperfusion. A 50 µL of samples from the abluminal side were collected at indicated time points. An equal volume of fresh medium was replaced to maintain the sink conditions. The concentration of TRITC-Dextran was measured using Synergy HTX multimode plate reader at excitation 485/20 and emission 580/50 nm. The diffusion rate of TRITC-Dextran at each time point was calculated as the amount of TRITC-Dextran present in the basolateral compartment per unit surface area of the insert per unit time.

$$Diffusion\ rate\ of\ TRITC-Dextran = \frac{Amount\ of\ TRITC-Dextran\ in\ basolateral\ compartment}{(Surface\ area\ of\ transwell\ insert)x(time\ at\ which\ basolateral\ sample\ was\ removed)} \quad \text{(Equation 2)}$$

2.15. Statistical analysis

Statistically significance among the mean of controls and treatment groups or within treatment groups were analyzed using one-way analysis of variance (ANOVA) or two-way ANOVA at 95% confidence intervals using GraphPad Prism 9 (GraphPad Software, LLC). The notations for the different levels of significance are indicated as follows: *p<0.05, **p<0.01, ***p<0.001, ****p<0.0001.

3. Results

3.1. EVs retained their physicochemical characteristics and membrane integrity upon revival from storage conditions. We jointly refer EXOs and MVs as EVs wherever applicable. We first studied the effect of storage conditions on the retention of physicochemical characteristics of hCMEC/D3-derived EXOs and MVs using dynamic light scattering (**Fig. 1**). Freshly isolated EXOs and MVs showed particle diameters of about 210 and 265 nm with dispersity indices ranging from 0.35 to 0.4 (**Fig. 1 a-d**). The average diameter of EXOs significantly ($p<0.05$) increased after the first freeze-thaw cycle (FT: samples were frozen at -20°C for 24 h followed and were thawed at room temperature for 30 min), however, there were no significant differences in the particle diameters of EXOs between the fresh sample and after three FT cycles (**Fig. 1a**). Similar to EXOs, MVs retained their particle diameters after three FT cycles with a consistent dispersity index (**Fig. 1b,d**). EXOs and MVs showed an initial negative zeta potential of about -22 mV that ranged between -15 to -30 mV during three consecutive FT cycles (**Fig. 1e,f**). More than 90% of EXOs and MVs (post-freeze-thaw cycles) showed a unimodal particle size distribution in the intensity plot (**Fig. S1**). Nanoparticle tracking analysis was also performed to measure particle diameter and concentration of freshly isolated EVs. The number-weighted mean diameters of EXOs and MVs were about 157 and 146 nm, respectively (**Fig. 1i**). The concentration of freshly isolated EXOs and MVs was ranged from 4.6 to 5.1 $\times 10^8$ particles per milliliter (**Fig. 1i**).

552 The membrane integrity of EVs during their storage conditions was determined using a

553 previously reported calcein-based flow cytometry assay (28) that allows distinguishing the

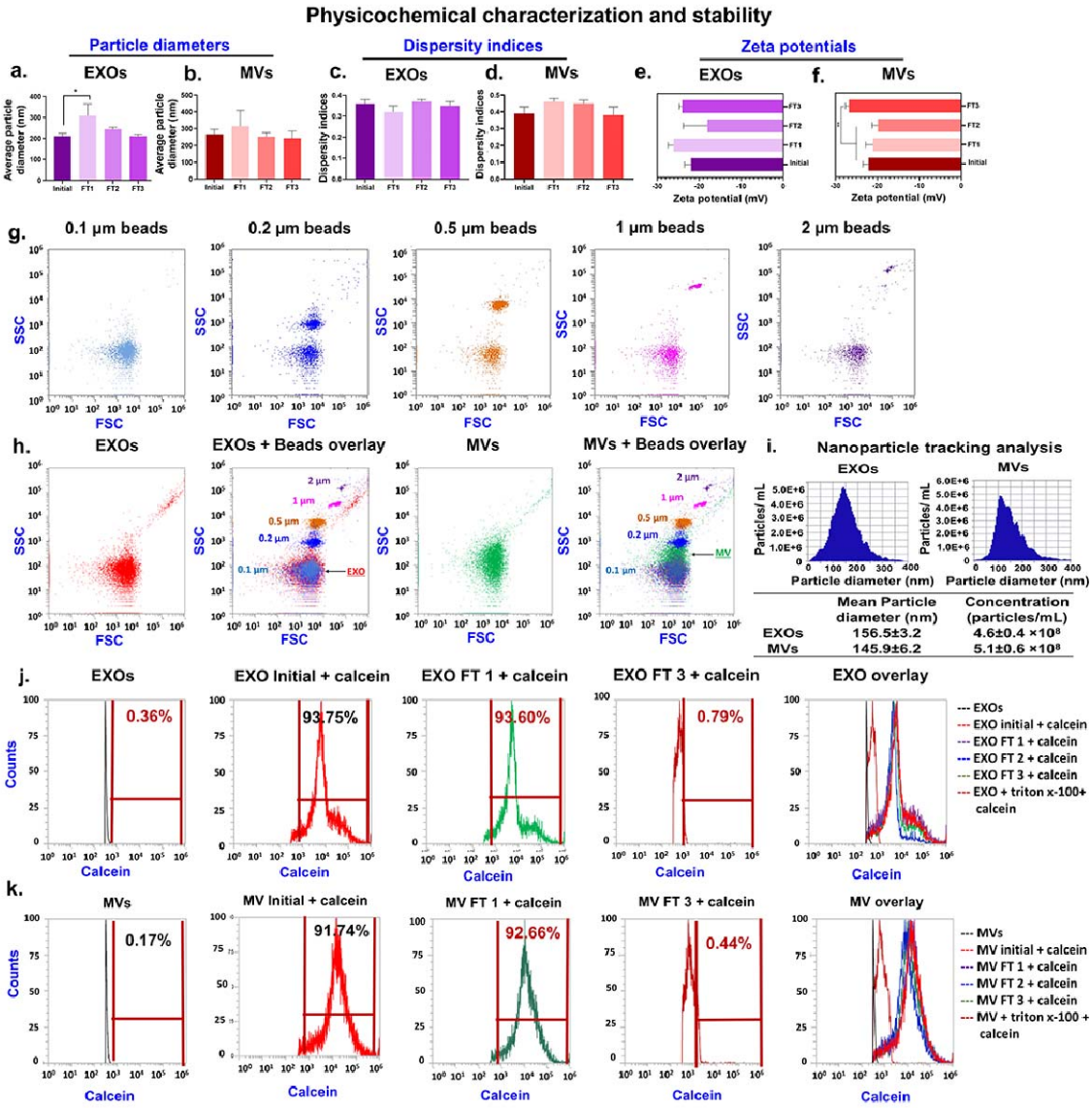

Fig. 1. Physicochemical characteristics and stability of EVs during storage conditions. Average particle diameters (**a,b**), and dispersity indices (**c,d**), and zeta potentials (**e,f**) of hCMEC/D3 cell line-derived EVs after three freeze-thaw (FT) cycles were determined using dynamic light scattering on a Malvern Zetasizer Pro-Red. Freshly-isolated samples (Initial) were used as controls. Samples were diluted to 0.5 mg protein/mL in 1x PBS for particle diameter and 10 mM HEPES buffer pH 7.4 for zeta potential measurements. The samples were stored at -20°C for 24 h and thawed at room temperature for 30 min prior to analysis. Data are presented as mean±SD of n=3 measurements. * $p<0.05$. The particle counts of polystyrene calibration beads, EXOs, and MVs were captured in forward scatter (FSC), side scatter (SSC) plots using Attune NxT flow cytometer (**g,h**). (**i**) EV particle diameter and concentration measurement using nanoparticle tracking analysis. The histograms of calcein-positive events of intact EXOs (**j**) and MVs (**k**) post-three FT cycles were detected using a small particle side scatter 488/10-nm filter in an Attune flow cytometer. Unstained EVs were used to gate the histograms for estimating percentage calcein-positive counts.

554 fraction of intact vs. disrupted vesicles based on the number of calcein-positive events in density

and histogram plots (**Fig. 1g-h, j-k**). Prior to analyzing the EVs, we first calibrated the flow cytometer using polystyrene beads of particle diameters ranging from 0.1 to 2 µm using a small particle side scatter filter (488/10 nm, BL1) (**Fig. 1g**). The relative position of EV clusters in the FSC/SSC overlay plots was directly proportional to the particle diameter since an increase in diameter showed a right-upward shift of the clusters. Notably, EXO and MV clusters overlapped to a large extent in the area corresponding to 0.1-0.2 µm bead diameters suggesting that this flow cytometry method allowed us to detect EV-sized particles (**Fig. 1h**). The particle counts for PBS/calcein AM, unlabeled-EXOs and MVs, PBS/Triton X-100/calcein AM mixture (sample processing controls) were acquired on SSC/BL1 density plots. Gates were created on the histogram and density plots to (1) distinguish the non-specific/background signals from PBS, calcein AM, and Triton X-100, and (2) measure the signal intensities of calcein-labeled EVs. About 90% of EXOs and MVs in freshly-isolated EV samples were calcein-positive suggesting that the EVs retained intact membranes after the ultracentrifugation and resuspension process (**Fig. 1j-k**). Importantly, >85-90% EXOs and MVs remained their membrane integrity after three consecutive freeze-thaw cycles confirming the lack of significant membrane damage during and upon revival from storage conditions. In addition, EVs lysed with Triton X-100 showed less than 10% calcein-positive particle counts demonstrating the specificity of calcein signal intensities associated with the intact EVs.

3.2 MVs contain mitochondria and transfer their mitochondrial load to recipient primary HBMECs and hCMEC/D3 cells. We studied the morphology of naïve EXOs and MVs isolated from hCMEC/D3 cells using transmission electron microscopy (TEM). TEM analysis of negatively-stained EVs showed nearly spherical EXOs of about 50 nm (**Fig. 2a**)

578 whereas MVs were ca. 200 nm structures (**Fig. 2b**). TEM images of sectioned EXOs showed

vesicles with particle diameters ranging from 20-100 nm and heterogeneous shapes (**Fig. 2c-e**). The core of EXOs appeared less dense and transparent suggesting that the core of EXOs may not contain organelles like mitochondria and may instead contain cytosolic components. TEM

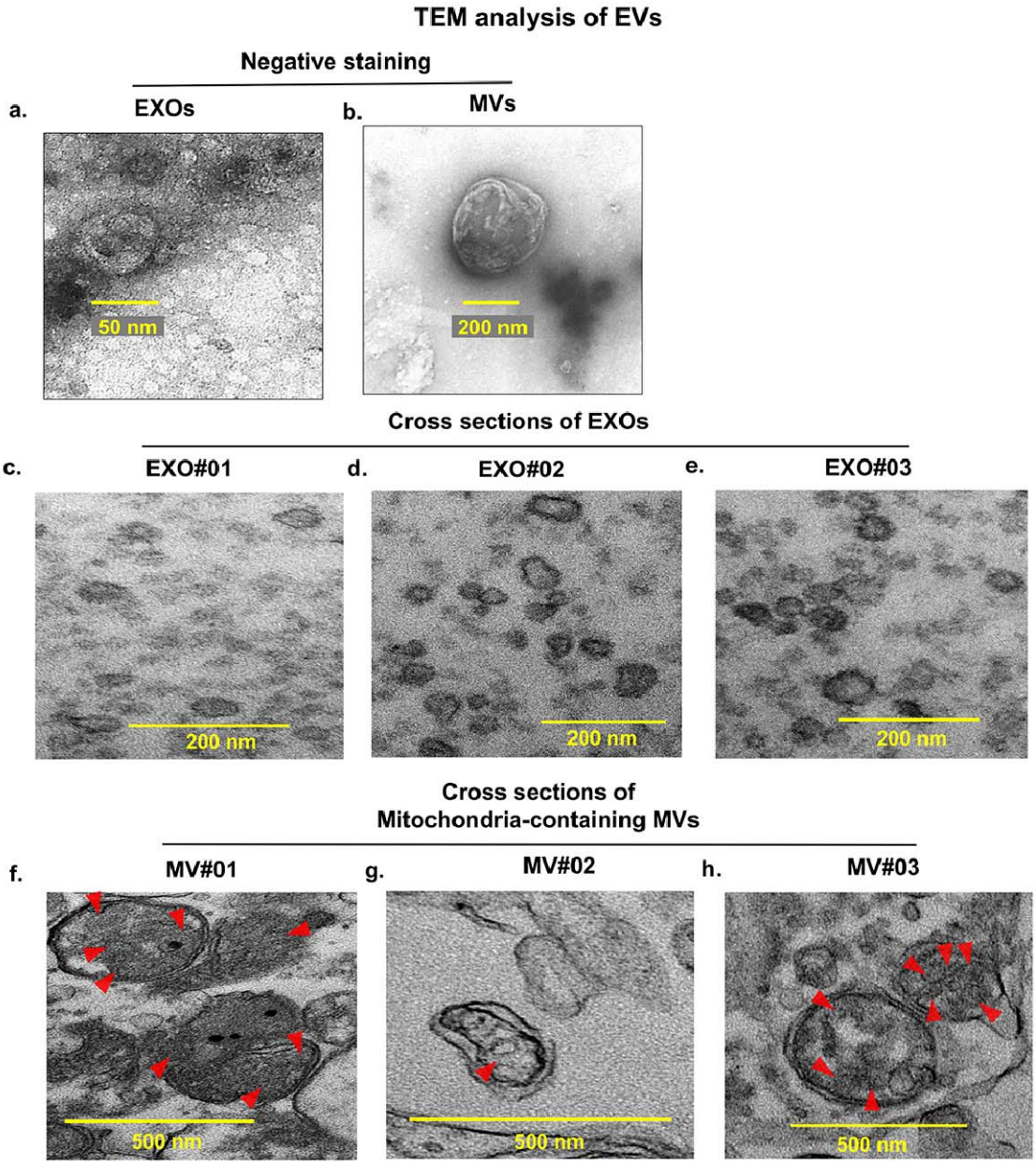

Fig 2. Transmission Electron Microscopy (TEM) analysis of EVs. (**a,b**) Negative stain TEM images of hCMEC/D3-derived EXOs (**a**) and MVs (**b**). (**c-e**) TEM images of sectioned EXOs and MVs (**f-h**). MVs show mitochondria.

images of sectioned MVs showed particle diameters ranging from about 150- 500 nm and heterogeneous shapes (**Fig. 2f-h)**. The core of MVs was highly dense and contained mitochondria (indicated by red arrowheads, **Fig. 2f-h**) ranging from one (**Fig. 2g**) to as many as five (**Fig. 2f,h**) mitochondria per MV. The presence of mitochondria in MVs was associated with the presence of mitochondrial cristae-like structures. It should be noted that a large number of MVs contained one/more mitochondria suggesting consistent incorporation of mitochondria in hCMEC/D3-derived MVs. Mitochondrial incorporation into MVs, but not EXOs may be explained by the fact that mitochondria undergo a series of dynamic changes, including biogenesis, shape changes, and selective degradation and rapidly transport along with cell bodies to extremities (37), and may subsequently be released via MVs.

Next, we wanted to determine if EVs can transfer their mitochondrial load into recipient HBMECs (**Fig 3a,b**). Therefore, we isolated EXOs and MVs from hCMEC/D3 cells pre-stained with Mitotracker Red (MitoT-red). Donor hCMEC/D3 cells were treated with MitoT-red-EXOs and MitoT-red-MVs at 30 to 150 µg EV protein/well for 72 h and MitoT-red signals in the recipient hCMEC/D3 cells were measured using flow cytometry. The intensity of MitoT-red-EVs in the recipient HBMECs (**Fig. 3a,b**) was analyzed using histogram plots. Untreated HBMECs cells were used as control and were gated for data analysis (**Fig. 3a,b**). Cells pre-stained with MitoT-red were used as a positive control and showed about 82% MitoT signals suggesting the presence of polarized mitochondria (**Fig. 3a,b**). Cells treated with unstained MVs did not show any MitoT-red signals in hCMEC/D3 cells suggesting the absence of non-specific MitoT signals (**Fig. 3a**). Cells treated with MitoT-red-MV at a low dose of 10 µg dose showed about 32% MitoT-positive signals suggesting efficient mitochondrial transfer into the recipient

605 HBMECs cells (**Fig. 3a,c)**. The fraction of cells showing Mito-T-+ve signals increased from

606 61% at 75 µg to 68% at 150 µg MV dose (**Fig. 3a,c**). EXOs at lower doses of 30 and 75 µg
607 protein per well showed <5% of mitochondrial transfer which was increased to only about 13%
608 at 150 µg dose (**Fig. 3b,c**). Cells treated with EV (EXO: MV 1:1) at 75 µg EV protein showed
609 about 54% MioT-red signal intensity suggesting that inclusion of MVs in the EV mixture
610 treatment increased mitochondrial transfer in hCMEC/D3 cells (**Fig. 3b,c**). As expected, MVs

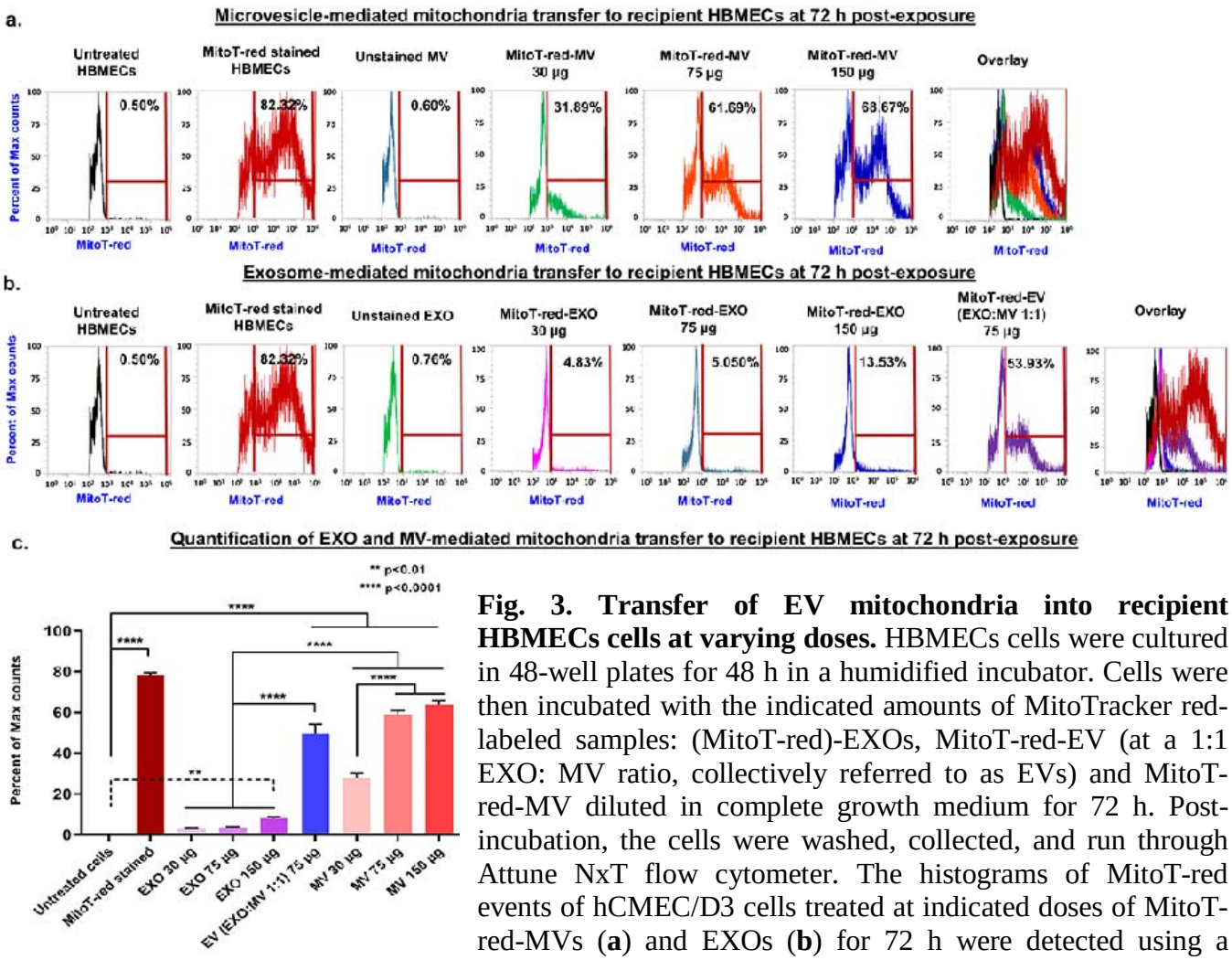

Fig. 3. Transfer of EV mitochondria into recipient HBMECs cells at varying doses. HBMECs cells were cultured in 48-well plates for 48 h in a humidified incubator. Cells were then incubated with the indicated amounts of MitoTracker red-labeled samples: (MitoT-red)-EXOs, MitoT-red-EV (at a 1:1 EXO: MV ratio, collectively referred to as EVs) and MitoT-red-MV diluted in complete growth medium for 72 h. Post-incubation, the cells were washed, collected, and run through Attune NxT flow cytometer. The histograms of MitoT-red events of hCMEC/D3 cells treated at indicated doses of MitoT-red-MVs (**a**) and EXOs (**b**) for 72 h were detected using a 674/10-nm side scatter filter in an Attune flow cytometer. Unstained EVs were used to gate the histograms for estimating percentage MitoT-red-positive counts. (**c**) Quantification of EXO and MV-mediated mitochondria transfer in recipient HBMECs at 72 h post-exposure. Data represent mean±SD of n=3.

showed a greater transfer of mitochondria into recipient HBMECs compared to EXOs consistent with the presence of notable mitochondrial load in MVs compared to EXOs (**Fig. 2c-h**).

We also studied EV-meditated mitochondrial transfer in recipient hCMEC/D3 cells (**Fig. S2**). Consistent with HBMECs, hCMEC/D3 cells treated with MitoT-red-MV showed a dose-dependent increase in mitochondrial transfer from 48% at 30 µg to 68% at 150 µg dose (**Fig. S2a**). We noted a dose-dependent increase in the mitochondrial transfer that increased from 13% at 30 µg EXO to about 33% at the 150-µg dose (**Fig. S2b**). EXO-mediated mitochondrial transfer in hCMEC/D3 cells was comparatively greater than primary HBMECs (**Fig. 3b and Fig. S2b**).

3.3. EVs transferred polarized mitochondria to recipient primary human brain endothelial cells (HBMECs). EVs are known to contain functional mitochondria, mitochondrial proteins, and mtDNA along with their vesicular content of lipids, nucleic acid, and proteins (38, 39). We hypothesized that mitochondrial load in naïve EVs can be internalized into and subsequently integrate with the mitochondrial network of the recipient endothelial cells. We first determined the uptake of EV-associated mitochondria in recipient primary HBMECs and hCMEC/D3 cells. The recipient HBMECs or hCMEC/D3 cells were treated with Mitotracker red-stained EVs (MitoT-red-EV) for 72 h prior to observing under an epifluorescence microscope. Prior to evaluating the uptake of MitoT-red-EVs, we evaluated the cytocompatibility of hCMEC/D3 cells treated with MitoT-red-EXOs and MitoT-red-MVs at different EV protein doses for 72 h and doses of 50 µg EV protein/well were well-tolerated by

633 the cells (**Fig. S3**). No MitoT-red-associated signals were observed in unstained/untreated
634 primary HBMECs
635

636 **Fig. 4. Transfer of EV mitochondrial load into the recipient HBMEC at varying doses and incubation times. (a)** HBMECs were cultured in 96-well plates until 80% confluency in a humidified incubator. Cells were then incubated with the indicated amounts of MitoTracker red-labeled samples: (MitoT-red)-EXO, MitoT-red-EV (at a 1:1 EXO: MV ratio, collectively referred to as EVs), MitoT-red-MV diluted in complete growth medium for 24, 48, and 72 h. Post-incubation, the cells were washed and incubated with phenol-red-free growth medium. Intracellular MitoT-red-EXO/EXO+MV/MV signals were observed under an Olympus IX 73 epifluorescent inverted microscope using Cy5 channel (purple puncta) at 20x magnification. Scale bar: 50 µm. **(b) Quantification of MitoT-red-EV uptake**. HBMECs were treated with the indicated samples and doses for 24, 48, and 72 h. At each time point, from each control and treatment group, at least three images were acquired and the total sum of grayscale signal intensities in the Cy5 channel were estimated using Olympus CellSens software. The measured intensities were normalized with those of the untreated cells.

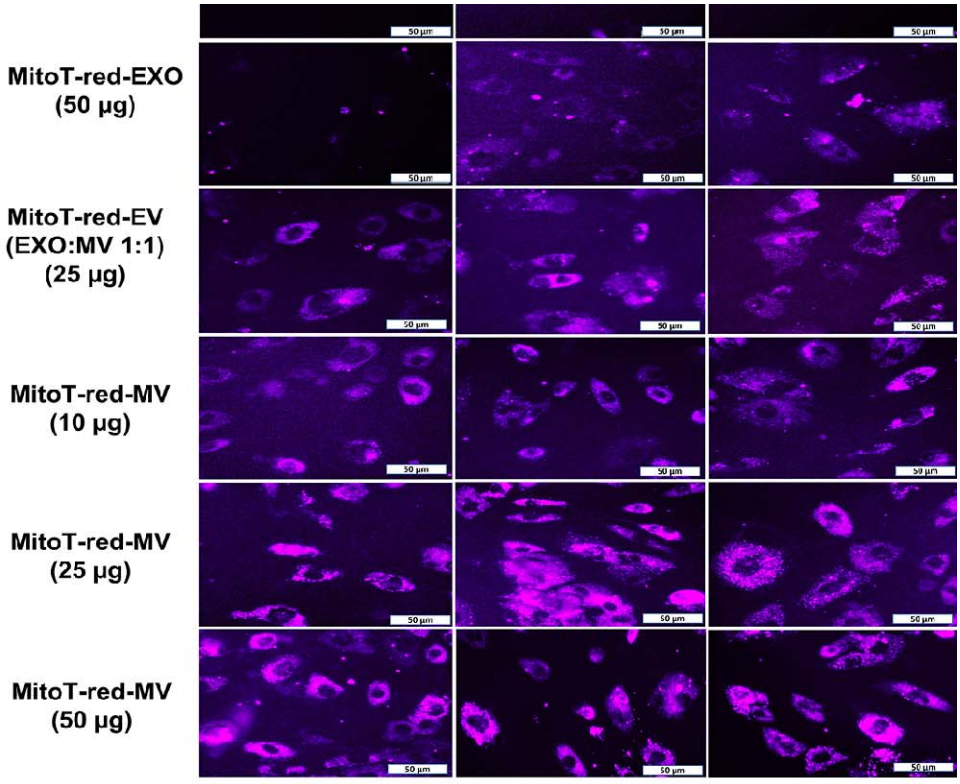

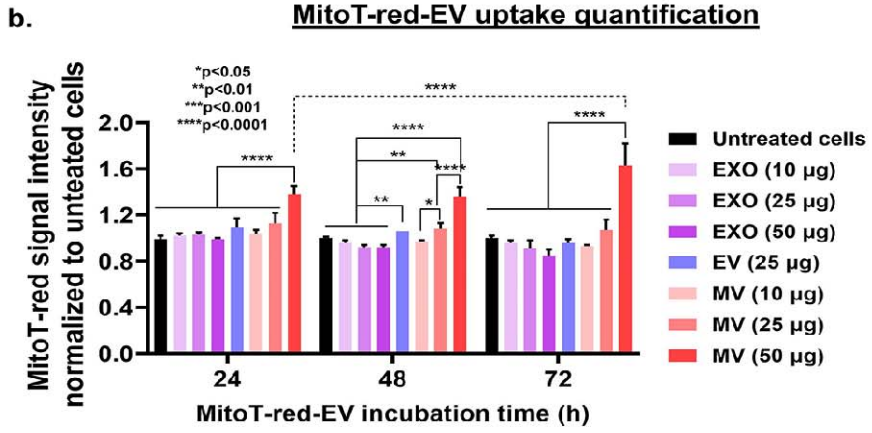

637 **4a**). MitoT-red-EXOs at 10 and 25 µg doses did not show positive signals in HBMECs for 48 h,
638 however, MitoT-red-EXOs at 50 µg doses showed faint intracellular Cy5 signals at 48 and 72 h
639 suggesting low levels of mitochondrial uptake after 48 h (**Fig 4a**). In contrast, strong intracellular
640 signals in HBMECs treated with MitoT-EXOs+MVs at the 25 µg (**Fig. 4a**) dose suggested that
641 the inclusion of microvesicles in the EV mixture led to an efficient uptake of polarized
642 mitochondria into HBMECs. Moreover, the increase in EXO+MV-mediated mitochondrial
643 transfer was statistically significant ($p<0.01$) at 48 h compared to EXOs alone (**Fig. 4b**).
644
645 Interestingly, MitoT-red-MVs at a dose as low as 10 µg showed efficient uptake in HBMECs
646 72 h post-exposure. The levels of uptake increased significantly ($p<0.0001$) as the dose of
647 MitoT-red-MVs increased from 10 to 50 µg at 48 h (**Fig. 4a,b**). The superior transfer of MV-
648 mediated mitochondria into HBMECs is likely due to a greater enrichment of functional
649 mitochondria with a full complement of mitochondrial proteins in MVs compared to EXOs.
650 Therefore, it can be expected that MVs may increase the cellular bioenergetics of the recipient
651 cells at lower doses compared to EXOs. We further confirmed the effect of dose and type of EV
652 subtype (MVs vs. EXOs) on the transfer of mitochondria into hCMEC/D3 cells (**Fig. S4a**).
653 Similar to the observations noted in the primary HBMEC cultures at 72 h post-exposure, EXOs
654 at 50 µg protein/well showed faint MitoT-red+ signals in the recipient hCMEC/D3 cells, whereas
655 cells treated with MVs showed a dose-dependent increase ($p<0.01$) in mitochondrial transfer
656 compared to EXO-treated endothelial cells (**Fig. S4a,b**).
657
658 **3.4. EV-transferred mitochondria integrated with the mitochondrial network in the**
659 **recipient endothelial cells**

We wanted to determine if the EV-mediated transfer of mitochondria integrated with the mitochondrial of the recipient cells. We isolated MitoT-red-stained polarized mitochondria from the donor cells as we did earlier in section 3.3. and the recipient cell mitochondria were stained using Mitotracker green (MitoT-green) and the overlap of these fluorescent signals was observed under an epifluorescent microscope. HBMECs and hCMEC/D3 cells pre-stained with Mitotracker green were incubated with MitoT-red-EXOs and MitoT-red-MVs at 10, 25, and 50 µg doses for 72 h. Cytosolic, diffuse MitoT-green signals were observed under the GFP channel whereas punctate MitoT-red EV signals were captured under the Cy5 channel (purple puncta). The pre-staining of HBMECs with Mitotracker green resulted in robust fluorescent signals for 72 h and incubation with Mitrotracker red-stained EVs did not affect the Mitotracker green fluorescence intensities.

The absence of GFP and Cy5 signals in untreated cells suggested the absence of non-specific signals at respective channel settings (**Fig. 5**). The cells pre-stained with MitoT-green alone showed green cytosolic signals associated with recipient mitochondria (**Fig. 5**). MitoT-red-MVs showed the greater intensity of Cy5 signals at all the tested doses compared to MitoT-red-EXOs,

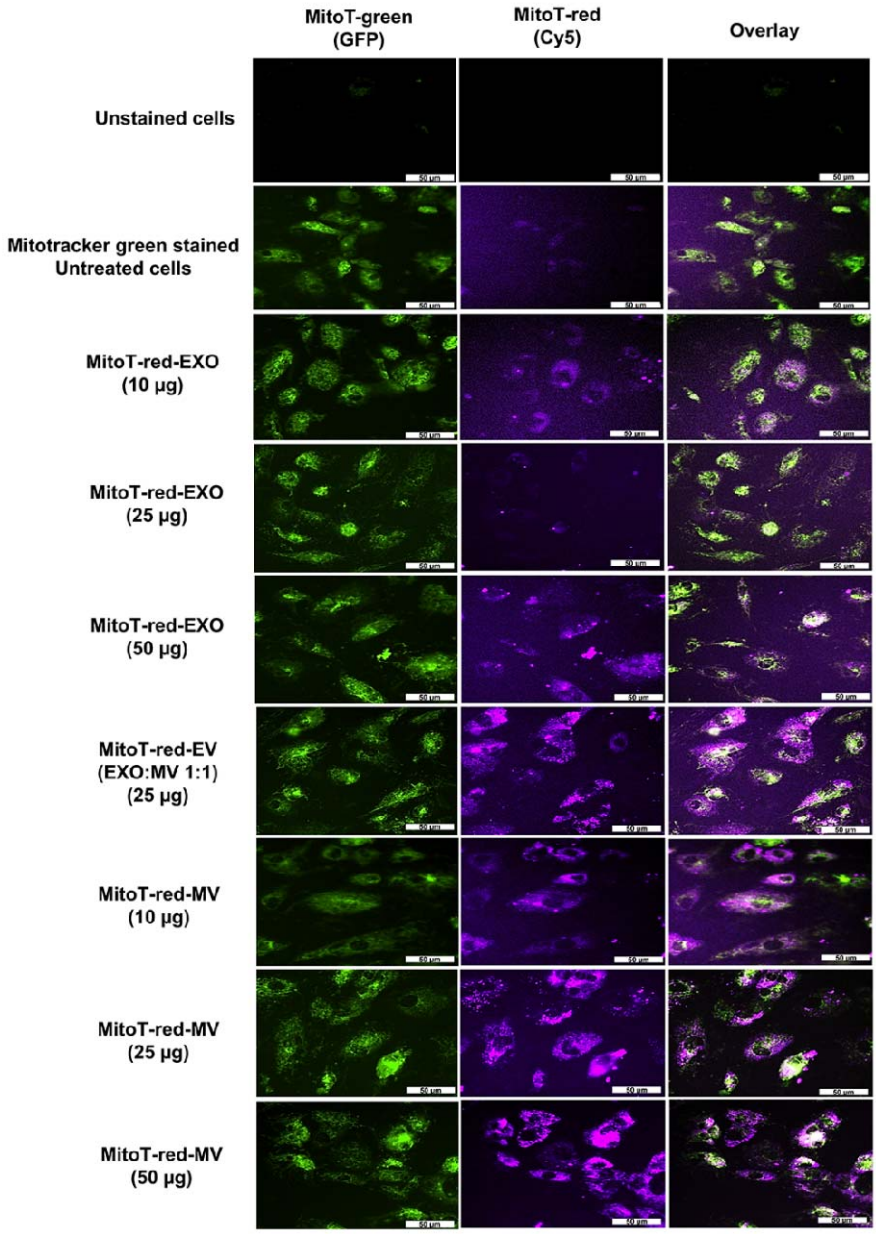

Fig. 5. Colocalization of EV mitochondrial load with the recipient HBMEC mitochondria. HBMECs were cultured in 96-well plates until 80% confluency in a humidified incubator. HBMECs were stained with Mitotracker Green for 30 min. Post-staining, the cells were washed and treated with the indicated doses of MitoT-red-EXOs, MitoT-red-EVs (at a 1:1 EXO: MV ratio, collectively referred to as EVs), and MitoT-red-MVs for 72 h. Untreated cells and cells stained with MitoTracker Green only were used as controls. Post-incubation, the treatment mixture was replaced with phenol-red-free growth medium. The Mitotracker green staining in recipient HBMEC was acquired using the GFP channel, whereas the purple fluorescence associated with EV-transferred mitochondrial load was captured using Cy5 channel in an Olympus IX 73 epifluorescent inverted microscope. Colocalization of the mitochondrial signals was confirmed by the presence of yellow signals

693 once again demonstrating that MVs contain a greater mitochondrial load that efficiently integrate
694 with the recipient cell's mitochondrial network compared to EXOs (**Fig. 5**). The overlay images
695 of recipient HBMEC mitochondria and EV-associated polarized mitochondria in the MV-treated

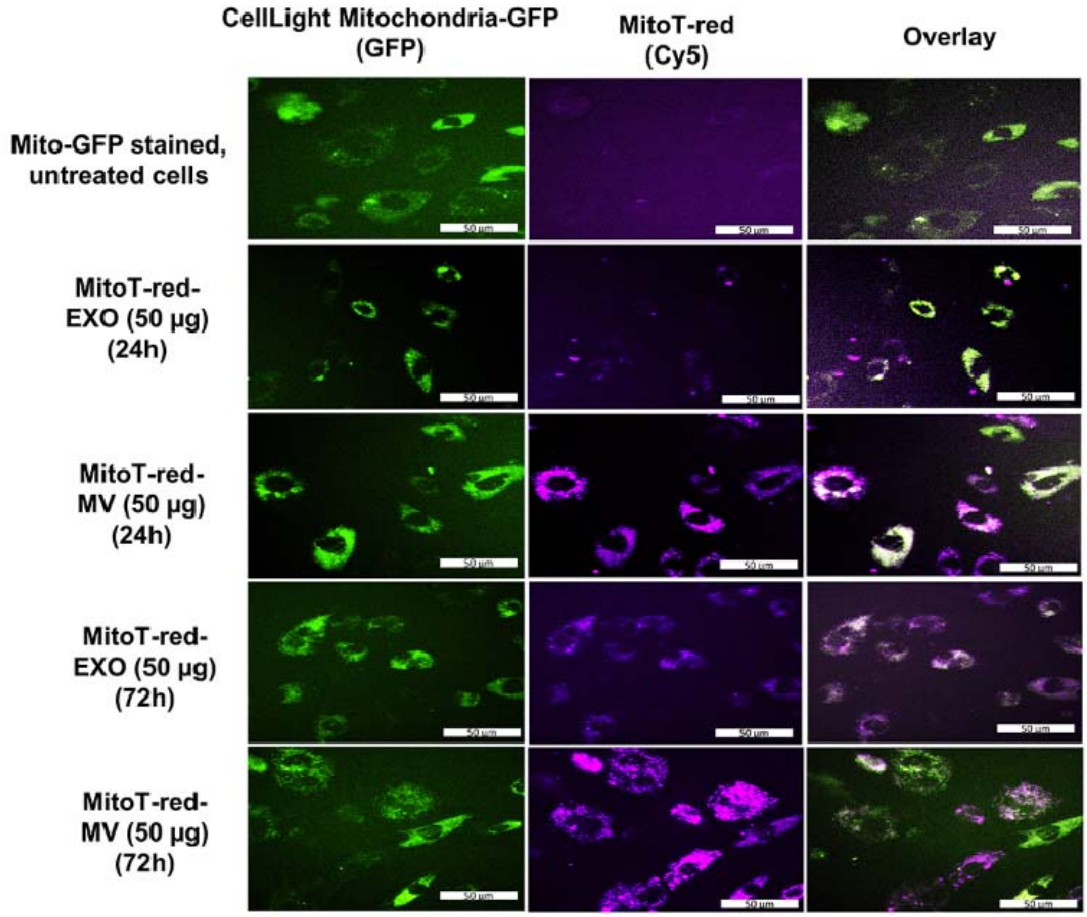

Fig. 6. Colocalization of EV mitochondrial load with the recipient HBMEC mitochondria using CellLight Mitochondria-GFP BacMam technique. Confluent HBMECs were transduced with CellLight Mitochondria-GFP at 2µL/10,000 cells for 16-18 h. The transduction mixture was then removed, cells were washed, and treated with a complete growth medium containing MitoT-red-EXO and MV at 50 µg/well for 24 and 72 h. Untreated cells and cells treated only with CellLight Mitochondria-GFP were used as controls. The green fluorescence associated with CellLight Mitochondria-GFP in recipient HBMECs was acquired using the GFP channel, whereas the purple fluorescence associated with polarized mitochondria from MitoT-red EXO and MV was captured using Cy5 channel using an Olympus IX 73 epifluorescent inverted microscope. Scale bar: 50 µm.

696 cells showed considerably higher colocalization compared to EXO-treated cells (**Fig. 5**). The
697 Pearson's correlation coefficient of GFP and Cy5 channel intensities demonstrated that EXO-

and MV- exposure resulted in a dose-dependent increase in colocalization (at least $p<0.05$), where MV exposure showed statistically significant ($p<0.0001$) and a greater degree of mitochondria colocalization compared to EXOs (**Fig. S5**). Similar to the primary HBMEC cultures, hCMEC/D3 cells pre-stained with Mitotracker green and treated with MitoT-red-MV showed a greater degree of colocalization indicated by the overlap of MitoT-green and MitoT-red compared to EXO-treated cells (**Fig. S6**).

We further confirmed the integration of EV-mitochondrial components with mitochondria of the recipient cells using an orthogonal technique that allowed us to confirm that the EV-transferred mitochondria (functional, polarized mitochondria) integrated with the structural protein-stained mitochondria in the recipient cells. CellLight Mitochondria-GFP BacMam is a fusion construct of α-pyruvate dehydrogenase (a mitochondrial matrix protein) and emGFP packaged in a baculoviral vector that allows specific tagging of a structural mitochondrial protein (40). HBMECs and hCMEC/D3 cells were first transduced with CellLight Mitochondria-GFP (CellLight-MitoGFP) before MitoT-red-EV treatment. Despite the low absolute frequency of transduction (40), the recipient endothelial cells showed a strong GFP fluorescence suggesting that CellLight-MitoGFP transduction effectively tagged the alpha pyruvate structural mitochondrial protein in HBMECs (**Fig. 6**) and hCMEC/D3 (**Fig. S7**) cells. Similar to Figure 5, MitoT-red-MV at a dose of 50 µg showed efficient transfer of mitochondria (purple puncta) in the recipient HBMECs and hCMEC/D3 cells. The EV MitoT-red puncta signals colocalized with recipient mitochondria (CellLight-MitoGFP) 72 h post-exposure. Notably, cells exposed to MitoT-red MV showed greater Cy5 signals compared to MitoT-red-EXO-treated cells confirming again that MVs contain a greater level of mitochondrial load compared to EXOs. The

Cy5 signal intensity in MV-treated cells was considerably increased at 72 h post-exposure compared to the 24 h time point suggesting that 72 h is an optimal exposure period for MV internalization into the recipient HBMEC and hCMEC/D3 cultures (**Fig. 6 and S7**). Importantly, the overlap of the structural protein-tagged recipient cell mitochondria with the functional MitoT-red-stained MVs indicates that the MV-delivered mitochondria undergo fusion with the recipient cell mitochondria. In conclusion, our data collectively demonstrate that microvesicles contained a greater mitochondrial load compared to exosomes and the MV-associated mitochondria integrate with the mitochondrial network in the recipient human brain endothelial cells. MV-mediated mitochondrial transfer increased with increasing doses of MVs and the greatest colocalization with the recipient endothelial cells was observed at a 50-µg dose and 72 h incubation time.

3.5. Naïve EVs increased HBMEC ATP levels under normoxic and hypoxic conditions.

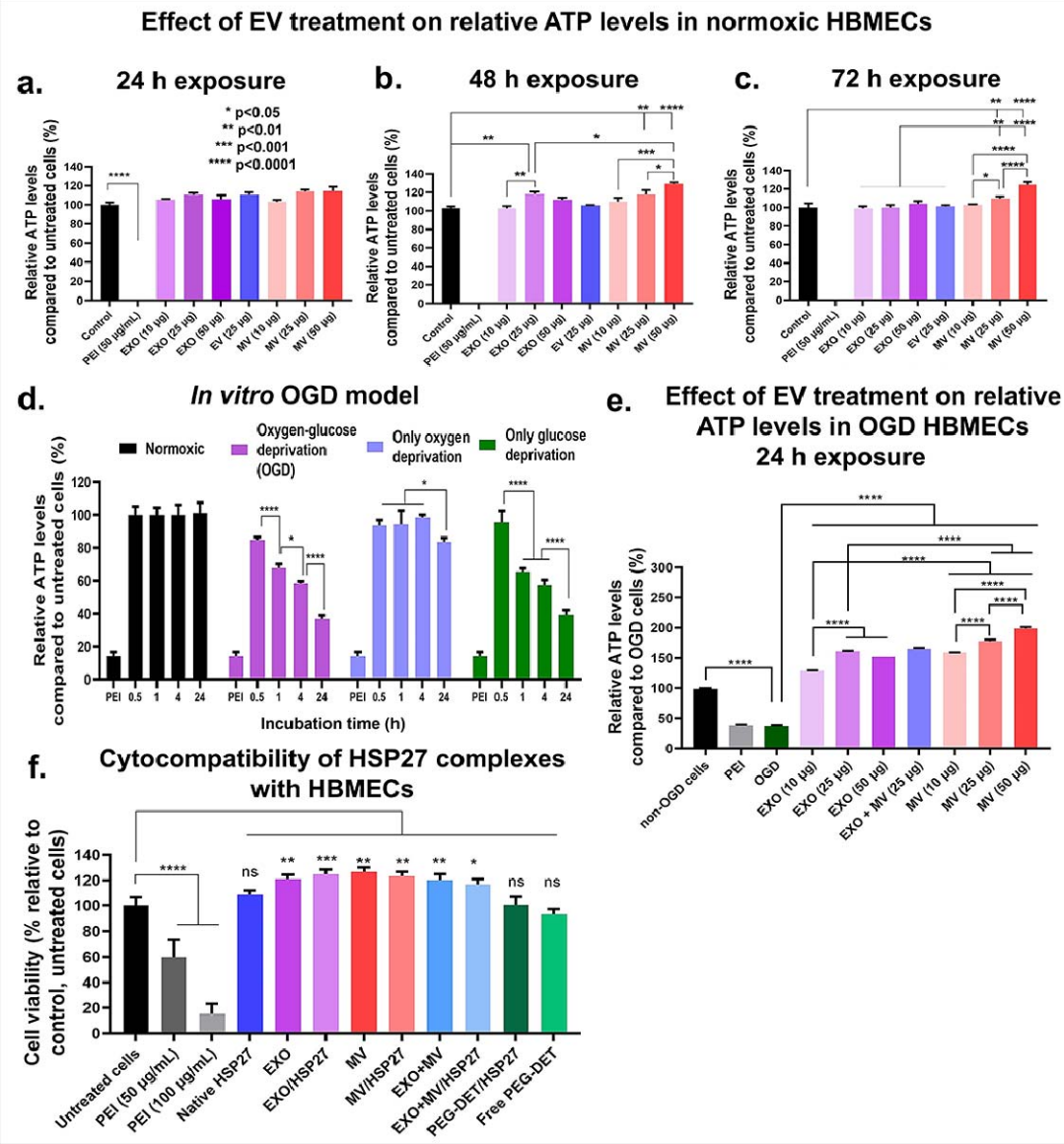

Fig. 7. EV-mediated increase in HBMEC ATP levels during normoxic and hypoxic conditions and cytocompatibility of polymer/HSP27 complexes with HBMEC. HBMEC cells were cultured in the 96-well plates until 80% confluency in a humidified incubator. (**a-c**) Confluent monolayers were treated with EXOs, MVs, and EVs (EXO: MV 1:1) at the indicated amounts for 24 (**a**), 48 (**b**), and 72h (**c**). Polyethyleneimine, PEI, at 50 µg/mL was used as a positive control for the ATP assay. Post-treatment, cells were incubated with a 1:1 mixture of fresh growth medium and Cell titer Glo reagent. The relative luminescence units (RLU) of the samples were measured using a SYNERGY HTX multimode plate reader at 1s integration time. Relative ATP levels were calculated by normalizing the RLU of treatment groups to the RLU of control, untreated cells. (**d**) Confluent normoxic HBMEC monolayers were treated with OGD medium and incubated in a hypoxic Billups-Rothenberg chamber at 37°C for 24 h. The following groups were also included: Normoxic HBMECs cultured in complete growth medium in a humidified incubator, oxygen-deprived cells cultured in complete growth medium in a hypoxic chamber, glucose-deprived cells cultured in OGD medium in a normoxic chamber. The cell viability of normoxic HBMECs was used as a control to calculate the cell viability in all treatment conditions. (**e**) Confluent HBMECs were treated with the indicated doses of EXOs and MVs in OGD medium and cell viability was measured 24 h post-treatment while untreated cells were used as a control. (**f**) Normoxic confluent HBMECs were treated with the indicated samples at a dose of 2 µg of HSP27 per well for 72 h before measuring cell viability. Data represent mean ±SD (n=3). * $p<0.05$, ** $p<0.01$, *** $p<0.001$, **** $p<0.0001$

The effect of hCMEC/D3-derived EVs on the ATP levels in recipient primary HBMECs were evaluated under normoxic conditions using an ATP assay. Primary HBMEC monolayers were treated with EXOs and MVs at 10, 25, and 50 µg EV protein per well for 24, 48, and 72 h. **Fig 7a** shows that the increase in HBMEC ATP levels upon EXOs and MVs treatment for 24 h was not statistically significant ($p>0.05$). Importantly, HBMECs treated at a dose of 25 µg EXOs for 48 h exposure showed a significant ($p<0.01$) increase in ATP levels compared to untreated cells. Interestingly, cells treated with MVs at 25 and 50 µg doses showed a dose-dependent and significant ($p<0.0001$) increase in relative ATP levels compared to untreated cells. In addition, the MV-mediated increase in ATP levels was significantly ($p<0.05$) higher compared to EXOs after 48 h exposure (**Fig. 7b**). At 72 h post-exposure, MVs at 25 and 50 µg doses showed a dose-dependent and significant ($p<0.01$) increase in relative ATP levels compared to untreated cells under normoxic conditions (**Fig. 7c**). In contrast, EXOs did not show any significant increase in relative HBMEC ATP levels compared to the control. In addition, MV-treated HBMECs showed

significantly higher ATP levels compared to EXOs at 72 h at all tested doses. The data suggested that the MV-mediated significant increase in relative ATP levels at 48 h (**Fig. 7b**) and 72 h (**Fig. 7c**) may likely be due to their inherent mitochondrial load—including mitochondria, mitochondrial DNA, and a full complement of mitochondrial proteins.

Ischemic conditions were simulated by culturing primary HBMECs under oxygen glucose-deprived (OGD), only oxygen-deprived, and only glucose-deprived conditions, and the resulting cell viability was evaluated from 0.5-24 h (**Fig. 7d**). HBMECs treated with complete growth medium and incubated in a humidified incubator (normoxic conditions) were used as a control for each time point. OGD HBMECs showed a time-dependent significant ($p<0.01$) decrease in cell viability compared to normoxic HBMECs. A four-hour OGD exposure led to about 40% cell death that further increased to about 60% at 24 h (**Fig. 7d**). Oxygen deprivation alone for 6 h did not result in a significant ($p>0.05$) decrease in cell viability, however, it caused nearly 20% cell death at 24 h. HBMEC cell viability decreased to about 60% during 2-6 h, followed by 50% cell viability at 24 h of glucose deprivation. To summarize, OGD-exposed HBMECs at 24 h showed a significant ($p<0.0001$) and maximum reduction in cell viability compared to other treatment conditions, therefore, we chose to expose HBMEC under OGD conditions for 24 h to simulate ischemic conditions for further experiments.

We studied whether naïve EXOs and MVs can increase the cell survival of OGD-exposed primary HBMECs. HBMECs in OGD medium were incubated with EXOs and MVs at 10, 25, and 50 µg EV protein/well for 24 h. The cell viability of EV-treated HBMEC cells was compared with untreated HBMECs maintained in OGD medium in a normoxic incubator (**Fig.**

769 **7e**). EXOs and MVs at all treated doses showed a significant ($p<0.0001$) increase in cell viability
770 compared to control, untreated HBMECs (**Fig. 7e**). In addition, an increase in EXO and MV
771 dose from 10 to 25 µg EV protein/well showed a significant ($p<0.0001$) increase in ATP levels.
772 HBMECs treated with MVs at 50 µg/well showed a maximum, ca. five-fold increase in ATP
773 levels compared to untreated cells. Importantly, MVs showed a significantly ($p<0.0001$) higher
774 HBMEC cell survival rate compared to EXOs at the same dose (25 and 50 µg) suggesting that
775 MVs outperformed EXOs in increasing HBMEC cellular energetics under ischemic conditions.
776 We also confirmed that the EV-mediated increase in endothelial cell viability under OGD
777 conditions in the hCMEC/D3 cell line (**Fig. S8a**). Consistent with primary human brain
778 endothelial cells, hCMEC/D3 cells treated with EXOs and MVs at 10, 25, and 50 µg EV
779 protein/well showed about a three to four-fold increase in endothelial ATP levels compared to
780 ischemic cells under hypoxic conditions. Moreover, the EV-mediated increases in ischemic
781 hCMEC/D3 cell survival were dose-dependent. Lastly, MV-treated ischemic hCMEC/D3 cells
782 showed a greater increase in ATP levels compared to EXO-treated cells (**Fig. S8a**).
783
784 **3.6. EVs increased the oxidative phosphorylation and glycolytic functions of recipient**
785 **endothelial cells under normoxic and hypoxic conditions**. The mitochondrial function of
786 hCMEC/D3 cells treated with EVs under normoxic conditions was evaluated using Seahorse
787 analysis by measuring oxygen consumption rate (OCR). hCMEC/D3 cells were treated with
788 EXOs and MVs at 3.4, 8.3, and 16.5 µg protein/well in complete growth medium for 24, 48, and
789 72 h. The basal OCR, maximum OCR, and proton leak at each time point were measured for
790 hCMEC/D3 cells treated with different doses of EXOs and MVs. Basal and maximum OCR was
791 not increased in EXO or MV-treated cells compared to untreated cells at 24 and 48 h (**Fig. 8a,b**).

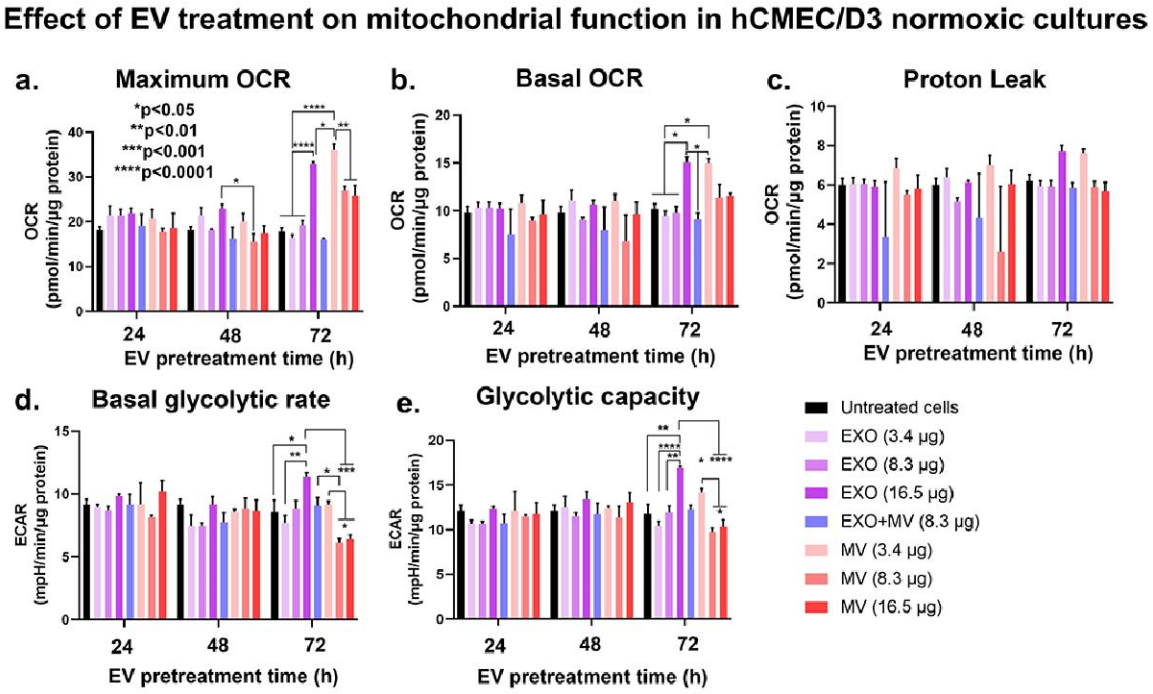

Fig. 8. Effects of EV exposure on mitochondria function in the recipient human brain endothelial cells under normoxic conditions. hCMEC/D3 cells were cultured in a Seahorse XF96 plate for 4 days at 20,000 cells/well. EXO, MV, and EV (EXO+MV; 1:1) were diluted in complete growth medium at the indicated doses of µg EV protein/well and cells were incubated in a humidified incubator for 24, 48, and 72 h. Post-treatment at each time point, the medium was replaced with DMEM and maximum oxygen consumption rate (OCR) (**a**), basal OCR (**b**), and proton leak (**c**) were measured using the Seahorse XFe96 analyzer. Basal glycolytic rate (**d**), and glycolytic capacity (**e**) were determined by measuring extracellular acidification rate (ECAR). Data represents mean±SEM (n=3). *p<0.05, **p<0.01, ***p<0.001, ****p<0.0001

In contrast, endothelial cells exposed to EXOs and MVs for 72 h showed a dose-dependent, significant ($p<0.0001$) increase in basal and maximum OCR compared to control, untreated cells, indicating that it takes 72 h for EV-mediated mitochondrial transfer and resulting increase in mitochondrial functions (**Fig. 7a-c and Fig. 4-6**). EXOs at 16.5 µg protein/well showed a significant ($p<0.0001$) increase in OCR compared to 3.4 and 8.3 µg protein/well EXO doses. Besides, MVs at 3.4 µg protein/well showed a maximum and significant ($p<0.0001$) increase in OCR compared to higher MV doses, and untreated cells. Importantly, MV-mediated increase in OCR was significantly ($p<0.05$) higher compared to the maximum EXO dose suggesting that

MVs outperformed EXOs in increasing the recipient endothelial cells' mitochondrial function under normoxic conditions. The MV-mediated increase in mitochondrial function was consistent with the MV-mediated increase in cell viability in ATP assay (**Fig. 7**), intracellular uptake of MV-associated mitochondria (**Fig. 4**), and the integration of MV-associated mitochondria with the recipient cell's mitochondrial network (**Fig. 5, 6**). Notably, EV exposure did not affect proton leak for 72 h under normoxic conditions (**Fig. 8c**).

We further evaluated the effects of EVs on non-mitochondrial energy generation pathways such as cytosolic glycolytic capacity in the recipient endothelial cells. Extracellular acidification rate (ECAR) is a key indicator of cellular glycolysis and can be determined in real-time by measuring free protons in a Seahorse plate transient microchamber (41). ECAR (basal glycolysis rate and glycolytic capacity) was measured in hCMEC/D3 cells treated with EXOs, MVs, and EVs (EXOs+MVs at 1:1 w/w) at 3.4, 8.3, and 16.5 µg EV protein/well in complete growth medium (**Fig. 8d,e**). We did not note any changes in the basal glycolysis rate and glycolytic capacity of hCMEC/D3 cells pre-treated with EXOs and MVs for 24 and 48 h compared to untreated cells. However, treatment with 16.5 µg EXOs for 72 h showed a significantly ($p<0.05$) greater basal glycolysis rate and glycolytic capacity compared to untreated cells. The glycolysis rate and glycolytic capacity of hCMEC/D3 cells were significantly ($p<0.01$) increased with an increase of EXO dose from 3.4 to 16.5 µg protein/well. Notably, EXOs outperformed in increasing glycolysis capacity and basal glycolytic rate compared to MVs.

The second goal of the present work was to evaluate the effects of HSP27 delivery on tracer permeability across the BBB in an OGD cell culture model of ischemia/reperfusion injury. We

formulated EVs (a cell-derived, natural carrier) and a synthetic cationic polymer, PEG-DET, for the delivery of exogenous HSP27 protein. Followed by physicochemical characterization of the formed mixtures/complexes, we evaluated their effects on the paracellular permeability of small and large molecular mass fluorescent tracers across primary HBMEC monolayers exposed to OGD.

3.7. Exogenous HSP27 protein formed complexes with PEG-DET, EVs, and PEG-DET-EV mixtures. The complexation of HSP27 protein with PEG-DET and hCMEC/D3-derived EVs was determined by studying the electrophoretic mobility of HSP27 in a native polyacrylamide gel electrophoresis (PAGE) setup. Native recombinant human HSP27 at the running buffer of pH 8.3 carries a net negative charge (estimated charge: -4.2 mV) (42), and therefore, migrated from the loading spot towards the anode during electrophoresis (**Fig. 9a**). First, the complexation efficiency of PEG-DET with HSP27 was studied by comparing the relative changes in HSP27 band densities at polymer: protein weight/weight (w/w) ratios ranging from 0.05:1 to 20:1 (**Fig. 9a,b**). Compared to native HSP27 (100%, **Fig. 9b**), the relative band density of PEG-DET/HSP27 complexes at w/w 0.2:1 was considerably reduced to about 43%. As the w/w ratios increased, there was a gradual and significant decrease in HSP27 band densities (**Fig. 9a,b**). At PEG-DET/HSP27 w/w 10:1 and 20:1, the mean HSP27 band density decreased to nearly 25% suggesting that PEG-DET formed electrostatic complexes with HSP27 at physiological pH. The free polymer did not show any non-specific staining until the 1:1 w/w ratio. Non-specific staining of free PEG-DET polymer was observed in the samples that contained an equivalent quantity polymer at w/w 5 and 10:1.

To determine if natural nanocarriers such as EVs can be formulated for the delivery of

847 exogenous HSP27, hCMEC/D3 cell-line derived EXOs and MVs were mixed with HSP27 at EV

protein/HSP27 protein w/w ratios of 5:1, 10:1, and 15:1 and the electrophoretic mobility of

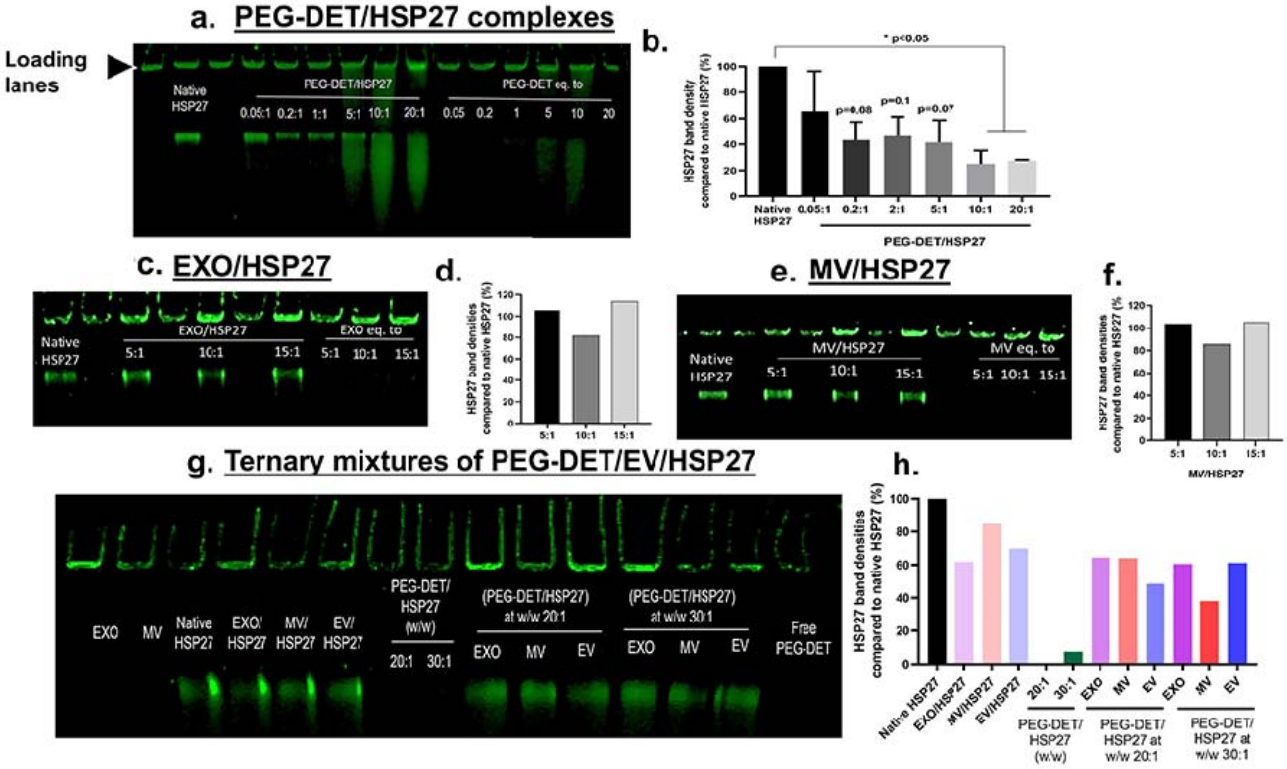

Fig. 9. Formation of EV- and PEG-DET/HSP27 complexes. (**a**) ***Native polyacrylamide gel electrophoresis (PAGE) for PEG-DET/HSP27 complexes***. Native HSP27, PEG-DET/HSP27 at indicated weight ratios, and free PEG-DET polymers were mixed with 1x native sample buffer and loaded in an SDS-free 4-10% polyacrylamide gel at 1 µg HSP27 per lane. (**c,e)** ***Native PAGE for hCMEC/D3-derived EV/HSP27 complexes: Native HSP27 and mixtures of EXO/HSP27*** (**c**), ***and MV/HSP27*** (**e**) at 5, 10, and 15:1 weight/weight (w/w) ratios were loaded in a SDS-free 4-10% polyacrylamide gel at 1 µg HSP27 per lane. Free EXOs and MVs equivalent to the amounts in 5:1, 10:1, and 15:1 w/w complexes were used as controls. (**g**) ***native PAGE for (PEG-DET/HSP27)/EV ternary mixtures***. PEG-DET/HSP27 complexes were prepared at 20:1 and 30:1 w/w ratios followed by incubation with 10 µg of EVs. The indicated samples were loaded in the gel at 1 µg HSP27/lane. Each gel was run at 100 V for 2 h and stained using Biosafe Coomassie G250. The gel was then scanned at 800 nm using an Odyssey imager at intensity setting 5. (**b,d,f,h**) Densitometry analysis was performed by measuring band densities of HSP27 in the different experimental groups in comparison to the band density of native HSP27 in the respective gel using Image Studio 5.0 software *p<0.05

HSP27 was studied using native PAGE (**Fig. 9c-f)**. Mixtures of HSP27 with hCMEC/D3 cell line-derived EXOs and MVs did not affect the migration of HSP27 at all tested weight ratios (**Fig. 9c,e**), however, EXO/HSP27 and MV/HSP27 mixtures at w/w 10:1 showed about a 20% reduction in HSP27 band density compared to native HSP27 (**Fig. 9d,f**). Despite the negative surface charges of EV and HSP27 that may result in electrostatic repulsion, the reduction in

HSP27 band density at the 10:1 w/w ratio suggested that HSP27 was stabilized by non-ionic/H-H bond-based interactions with the EVs. It should be noted that free EXOs and MVs equivalent to different weight ratios (present in the EV/protein mixtures) did not show Coomassie signals suggesting that EV membrane and intravesicular proteins exerted minimum interference in the detection of the observed protein bands.

We then formulated ternary mixtures of PEG-DET/HSP27 complexes with hCMEC/D3-derived EVs, and the resulting changes in HSP27 band intensity were studied using native PAGE followed by densitometry analysis (**Fig. 9g,h**). EXOs, MVs, and EV/HSP27 at w/w 10:1 showed about 20-40% reduction in band density whereas PEG-DET/HSP27 at w/w 20:1 and 30:1 showed >90% HSP27 complexation compared to native HSP27 (**Fig. 9h**). The HSP27 band density was decreased by 40-50% when PEG-DET/HSP27 at w/w 20:1 were incubated with 10 µg of EXOs, MVs, and EXO+MV 1:1 (EV). The % extent of reduction in HSP27 band density of (PEG-DET/HSP27)/EV complexes ranged among the values noted in the case of PEG-DET/HSP27 and EV/HSP27 complexes suggesting the competitive binding of negatively-charged EVs and HSP27 with the positively charged PEG-DET. Besides, increasing the relative amounts of PEG-DET in (PEG-DET/HSP27)/EV complexes further reduced HSP27 band density indicating the PEG-DET-mediated increase in complexation between HSP27 and EVs. To summarize, HSP27 formed electrostatic complexes with PEG-DET, non-ionic and weak interactions with hCMEC/D3-derived EVs, and ternary mixtures with both PEG-DET and HSP27: (PEG-DET/HSP27)/EVs.

3.8. Physicochemical characterization of the formed HSP27 complexes/mixtures

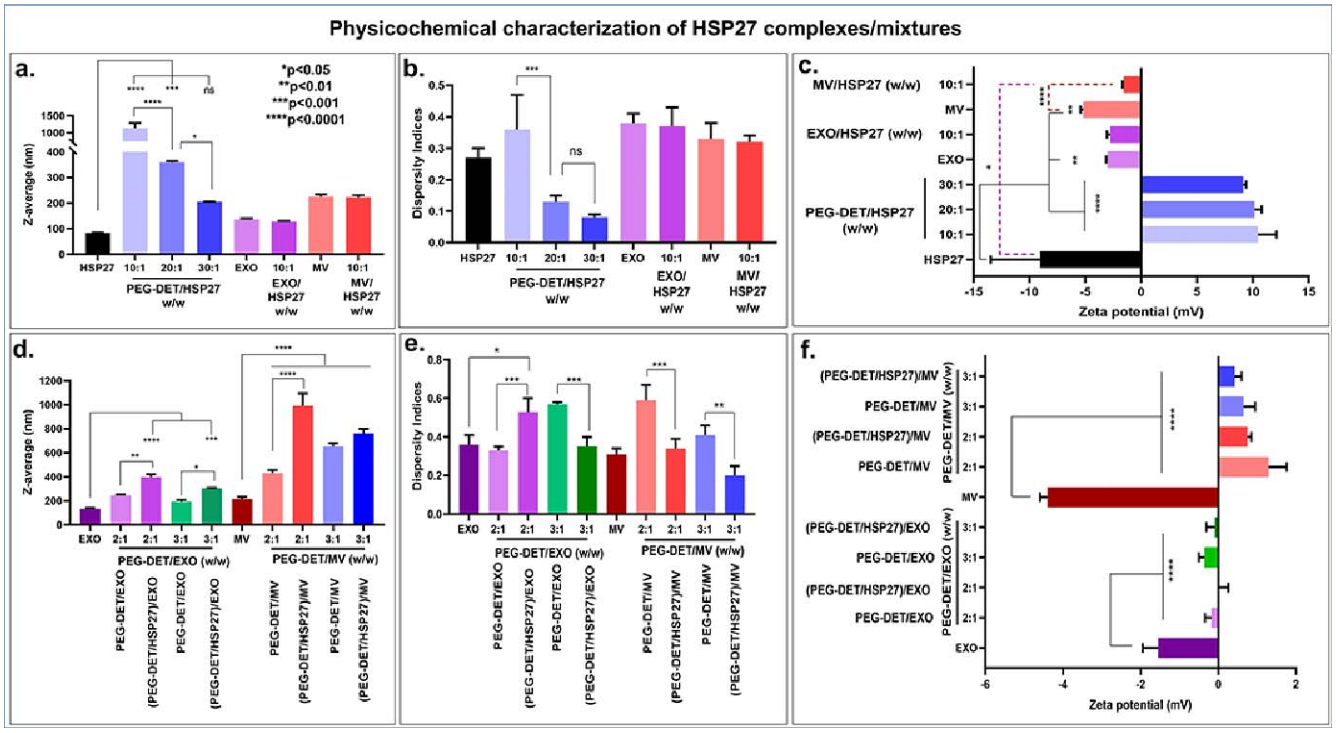

Fig. 10. Physicochemical characterization of HSP27 complexes with PEG-DET and EVs. Average particle diameters (**a**), dispersity indices (**b**), and zeta potentials (**c**) of the indicated samples were measured using dynamic light scattering on a Malvern Zetasizer Pro-Red. Average particle diameters (**d**), dispersity indices (**e**), and zeta potentials (**f**) of PEG-DET/EV and (PEG-DET/HSP27)/EV complexes at the indicated weight ratios. The samples containing 1 µg HSP27 protein were diluted to 50 µL in 10 mM HEPES buffer pH 7.4 for particle diameter measurements. The diluted samples were further diluted to 800 µL in 10 mM HEPES buffer pH 7.4 for zeta potential measurements. Data represent mean±SD (n=3). * p<0.05, **p<0.01, ***p<0.001, ****p<0.0001

Particle diameters, dispersity indices, and zeta potentials of the formed complexes/mixtures were measured using dynamic light scattering (**Fig. 10**). The average diameter of native HSP27 protein was about 85 nm with a dispersity index of 0.27 (**Fig. 10a,b**). The average zeta potential of native HSP27 (1 µg/mL in 10 mM HEPES buffer, pH 7.4) was about -9 mV suggesting that HSP27 exerts net negative surface charge under physiological conditions (**Fig. 10c**).

The average particle diameter of PEG-DET/HSP27 complexes at 10:1 w/w ratio was over 1000 nm with a broad dispersity index. As the weight ratio increased from 20:1 to 30:1, the particle diameter significantly ($p<0.05$) decreased from about 359 nm to 205 nm with a very

narrow dispersity index (**Fig. 10a,b**). PEG-DET/HSP27 complexes showed a unimodal particle size distribution in the intensity plots (**Fig. S9a**). PEG-DET/HSP27 complexes at 10:1 w/w ratio shifted the zeta potential of the native HSP27 protein from -9 mV to +10 mV confirming the electrostatic complexation of PEG-DET with HSP27. The zeta potentials, however, did not continue increasing for w/w ratios of 20:1 and 30:1.

EXOs and MVs derived from hCMEC/D3 cell lines showed diameters of about 136 and 225 nm respectively, with dispersity indices ranging from 0.3 to 0.4 (**Fig 10a,b**). EXOs showed a bimodal particle size distribution compared to MVs (**Fig. S9c,e**). EXO/HSP27 or MV/HSP27 mixtures at 10:1 w/w ratio did not change the average particle diameter and dispersity index compared to naïve EVs (**Fig. 10a,b**). In addition, the zeta potential of EXOs and MVs were -3.01 and -5.20 mV respectively (**Fig. 10c** and **Fig. S9d,f**). The zeta potential of MV/HSP27 mixtures shifted towards near-neutral values compared to naïve MVs and native HSP27 protein suggesting the formation of MV/HSP27 complexes (**Fig. 10c)**.

Next, PEG-DET was mixed with EXOs and MVs at PEG-DET/EV w/w ratios 2:1 and 3:1, and the resulting changes in particle sizes, dispersity indices, and zeta potentials were compared with naïve EXOs and MVs (**Fig. 10d-f**). The complexation of PEG-DET to EXOs showed a considerable increase in particle size from 134 nm to 245 nm without affecting the dispersity index (**Fig. 10d,e**). The shift in mean zeta potential from -1.55 mV to -0.18 mV suggested the electrostatic interactions of PEG-DET and EXOs (**Fig. 10f**). Furthermore, the z-average particle diameter of (PEG-DET/HSP27)/EXO significantly ($p<0.01$) increased to about 400 nm with a neutral zeta potential suggesting the interactions of PEG-DET/HSP27 and EXOs (**Fig. 10d,f**). A

similar trend was observed for MVs where the particle diameter was gradually and significantly ($p<0.0001$) increased from naïve MVs (216 nm), PEG-DET/MV (431 nm), and (PEG-DET/HSP27)/MV (991 nm) with dispersity indices ranging from 0.3-0.6 (**Fig. 10d,e**). A marked shift in zeta potential was observed from -4 mV for naïve MVs to 1.29 mV for PEG-DET/MVs, and 0.75 mV for (PEG-DET/HSP27)/MVs confirming the electrostatic interactions of PEG-DET and MVs (**Fig. 10f**). In addition, an increase in PEG-DET to EV w/w ratio from 2:1 to 3:1 showed a reduction in z-average diameter with a narrow dispersity index (**Fig 10d,e**). A slight decrease in zeta potential at PEG-DET/EV w/w 3:1 weight ratio suggested that increasing PEG-DET amount may increase the extent of complexation with EVs (**Fig. 10f**). The representative distribution plots of PEG-DET/EVs and (PEG-DET/HSP27)/EVs were shown in **Fig. S10**. To summarize, PEG-DET/HSP27 complexes showed a w/w ratio-dependent decrease in particle diameter with narrower dispersity indices and a positive surface charge. EV/HSP27 mixtures showed physicochemical characteristics more or less similar to naïve EVs. The observed changes in particle diameter, dispersity index, and zeta potential of (PEG-DET/HSP27)/EVs confirmed the complexation of EVs with PEG-DET/HSP27 complexes.

3.9. PEG-DET/HSP27 complexes and EV/HSP27 mixtures were cytocompatible with primary human brain endothelial cells.

We performed an ATP assay on primary HBMECs treated with native HSP27, MV, or EXO/HSP27 mixtures at w/w 10:1 and PEG-DET/HSP27 complexes at w/w 20:1 at a dose of 2 µg HSP27 per well. The cell viability of treatment groups was calculated using *Equation 1*. The average viability of cells treated with native HSP27 was 108.7% and there were no significant ($p>0.05$) differences between control, untreated cells, and native HSP27-treated groups

suggesting that native HSP27 at 2 µg/well was well tolerated by HBMEC under normoxic conditions for 72 h (**Fig. 7f**). The cell viability of HBMECs increased significantly ($p<0.01$) when treated with EXO/HSP27 (124.7%), MV/HSP27 (123.1%), and EXO+MV /HSP27 (116.8) mixtures at 10:1 w/w ratio compared to untreated cells suggesting that EV/HSP27 mixtures were well tolerated by HBMEC for 72 h (**Fig. 7f**). The EV/HSP27 mixture-mediated increase in cell viability can be correlated with a significant increase in HBMEC ATP levels that was observed when cells were treated with naïve EXOs (121%), MVs (126.4%), or EXOs+MVs (120.1%) at amounts equivalent those present in the EV/HSP27 mixtures. HBMECs treated with PEG-DET/HSP27 complexes at w/w 20:1 treated showed an average 100.4% cell viability suggesting that PEG-DET/HSP27 complexes were cytocompatible for 72 h. Free PEG-DET polymer was also well tolerated by HBMECs for 72 h. Polyethyleneimine, a positive control, at 50 and 100 µg/mL concentrations showed a significant ($p<0.0001$) reduction in HBMEC viability indicating that the assay was responsive to the toxicities. We also confirmed the cytocompatibility of HSP27 complexes with the hCMEC/D3 cell line (**Fig. S8b**). hCMEC/D3 monolayers treated with native HSP27, EXOs or MV/HSP27, and PEG-DET/HSP27 complexes treated showed >95% cell viability for 72 h demonstrating their cytocompatibility (**Fig. S8b**).

3.10. HSP27 complexes ameliorated the hypoxia-induced increase in BBB permeability in primary HBMECs

3.10.1. Paracellular permeability of 65-85 kD TRITC-Dextran (a large molecule tracer) in PEG-DET/HSP27 and EV/HSP27 pre-treated HBMECs. The effect of HSP27 complexed with PEG-DET and hCMEC/D3-derived EVs on the paracellular permeability of 65-85kD

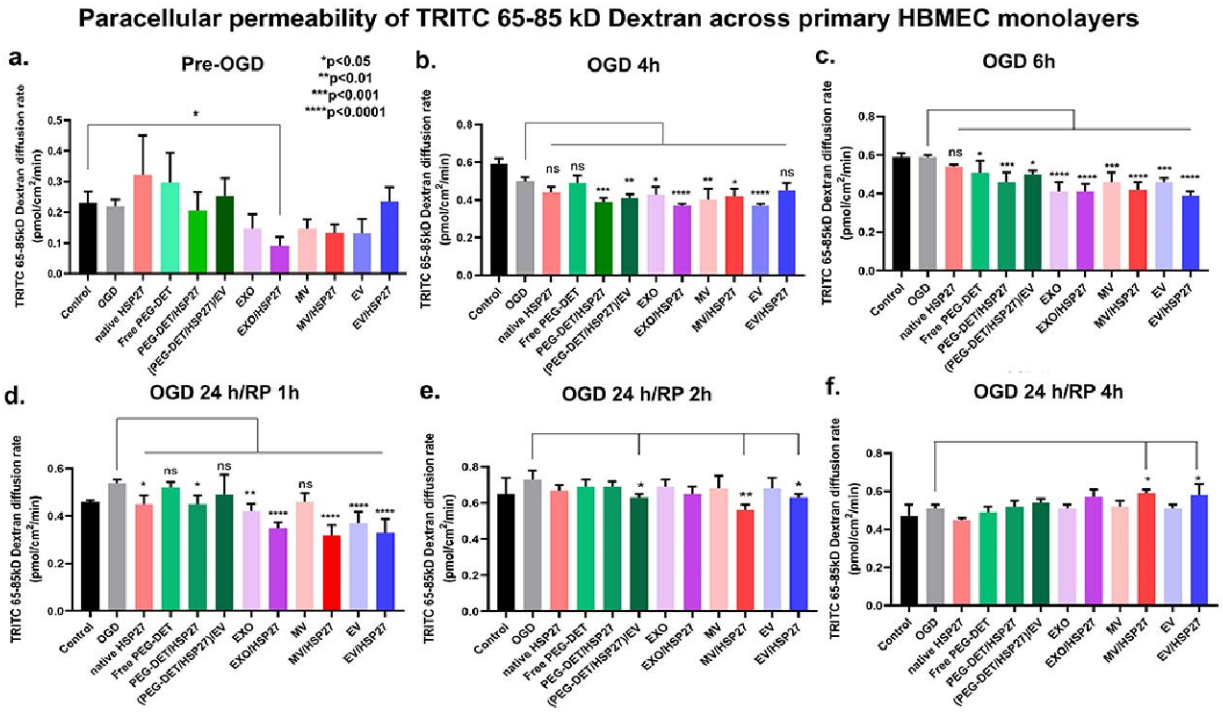

Fig. 11. Paracellular permeability of TRITC 65-85 kD Dextran under pre-OGD, OGD, and OGD/reperfusion conditions in HBMEC transwell culture inserts pre-treated with PEG-DET/HSP27 and EV/HSP27. HBMECs were seeded in 24-well plates and maintained in a 37°C humidified incubator for a week. The complete growth medium was replaced with 300 µL of growth media containing indicated treatment groups for 72 h. Post-incubation, the media was replaced with complete growth medium containing 1µM TRITC 65-85 kD Dextran for 1 h (Pre-OGD) **a**). Post-treatment, the treatment media was replaced with 300 µL of OGD medium containing 1 µM TRITC 65-85 kD Dextran for 24 h. The abluminal chamber was filled with 0.5 mL of complete growth medium. Control, untreated cells were incubated in complete growth medium in a humidified incubator whereas OGD treatment groups were incubated in an OGD chamber. At 4 (**b**) and 6 h post-OGD (**c**), a 500 µL volume was collected from the abluminal chamber and a fresh medium was added to the transwell inserts. Post-OGD treatment, HBMEC cells were washed with PBS and incubated with 300 µL of complete growth medium containing 1µM TRITC 65-85 kD Dextran and incubated in a humidified incubator for 1-24h. At each time point, a 500 µL volume was collected from the abluminal chamber and fresh medium was added to the transwell inserts. The concentration of TRITC 65 kD Dextran was measured at 1 h (OGD/RP 1h, **d**), 2 h (OGD/RP 2h, **e**), and 4 h (OGD/RP 4h, **f**) using a Synergy HTX multimode plate reader at 485/20 nm excitation and 580/50 nm emission settings. The diffusion rate of TRITC 65-85 kD Dextran at each time point was calculated by normalizing the amount of TRITC Dextran per unit surface area of the insert per unit time. Data represent mean±SD (n=2). * p<0.05, ** p<0.01, *** p<0.001, **** p<0.0001, ns: non-

TRITC-Dextran was evaluated using primary HBMECs seeded in transwell cell culture inserts under normoxic and hypoxic/OGD conditions. The 65-85kD TRITC-Dextran was used a high molecular mass tracer simulating the diffusion of large molecules through the damaged BBB (9)

and the effects of HSP27 delivery on decreasing the tracer diffusion rate. HBMECs were treated with HSP27 at a dose of 2 µg/well complexed with PEG-DET at 20:1 w/w ratio and EXOs, MVs, EVs (EXO: MV=1:1) at 10:1 w/w ratio. Native HSP27, free PEG-DET, and naïve EXOs, MVs, and EVs were used as controls. Prior to subjecting cells to OGD (Pre-OGD) (**Fig. 11a**), cells treated with EXO/HSP27 mixtures showed a significant ($p<0.05$) reduction in TRITC-Dextran permeability compared to control, untreated cells. In addition, naïve EXOs, MVs, and EVs showed a considerable decrease in 65-85 kD TRITC-Dextran permeability (**Fig. 11a**). The data suggested that naïve EXOs and MVs and their HSP27 mixtures may increase the barrier properties of endothelial tight junctions compared to untreated cells under normoxic conditions. Interestingly, cells treated with native HSP27 and PEG-DET/HSP27 complexes did not show any change in the TRITC-Dextran diffusion rate under normoxic conditions.

HBMECs pre-treated with PEG-DET/HSP27 complexes showed a significant ($p<0.001$) reduction in 65-85kD TRITC-Dextran diffusion during 4 h OGD exposure, whereas native HSP27 and free PEG-DET did not affect the permeability of high molecular weight dextran (**Fig. 11b**). EXO/HSP27 and MV/HSP27 mixtures showed a significant ($p<0.0001$) reduction in 65-85 kD dextran diffusion rate compared to untreated OGD cells. Naïve EXOs, MVs, and EVs also showed a statistically significant ($p<0.05$) reduction in dextran permeability under OGD conditions compared to untreated, OGD control (**Fig. 11b**). (PEG-DET/HSP27)/EV complexes also showed significant ($p<0.01$) reduction in 65-85 kD TRITC-Dextran diffusion rate compared to untreated cells at 4 h OGD. Exposure of cells to PEG-DET/HSP27, EXO/HSP27, MV/HSP27, EV/HSP27, and (PEG-DET/HSP27)/EV complexes continued to decrease HBMEC permeability at 6 h OGD exposure showing a significant ($p<0.0001$) reduction in the 65-85 kD diffusion rate

compared to the control (**Fig. 11c**). Importantly, naïve EXOs, MVs, and EVs also showed a significant ($p<0.0001$) reduction in 65kD TRITC-Dextran paracellular diffusion rate compared to control (**Fig. 11c**). The data suggested that PEG-DET/HSP27 complexes can limit the diffusion of large molecules post-hypoxia/ischemia. Importantly, naive EXOs and MVs limited the dextran diffusion before and during oxygen-glucose deprived conditions, whereas complexation of HSP27 with these EVs showed a synergistic effect on decreasing dextran diffusion during hypoxia/ischemia. Notably, there was no difference in the 65-85 kD TRITC-Dextran diffusion rate between control and HBMECs treated with HSP27 complexes at 24 h of OGD exposure (**Fig. S11a**).

Post-OGD, the OGD medium was replaced with fresh complete growth medium to evaluate the effect of HSP27 complexed with PEG-DET and EVs on the ischemia/reperfusion-mediated diffusion of 65kD TRITC-Dextran. Exposure of cells to PEG-DET/HSP27 complexes showed a significant ($p<0.05$) reduction in dextran diffusion rate 1 h post-ischemia/reperfusion (**Fig. 11d**). Importantly, EXO/HSP27, MV/HSP27, and EV/HSP27 mixtures showed a significant ($p<0.0001$) reduction in dextran diffusion rate compared to OGD control after 1 h ischemia/reperfusion. Moreover, naïve EXOs and EVs also showed significant ($p<0.05$) reduction in diffusion after reperfusion suggesting that naïve EVs increase brain endothelial tight junction integrity immediately after ischemia/reperfusion, and their mixtures with HSP27 synergistically reduce the large molecule infiltration across the brain endothelial cells (**Fig. 11d**). MV/HSP27 and EV/HSP27 mixtures showed a significant ($p<0.05$) reduction in diffusion rate compared to OGD control 2 h post-ischemia/reperfusion, whereas the changes in the diffusion rate of dextran were insignificant ($p>0.05$) in other treatment groups compared to OGD control

(**Fig. 11e**). It can be inferred that in addition to the naïve EV-mediated protection of BBB integrity pre-OGD/normoxia, during-OGD, and ischemia/reperfusion, their mixtures with HSP27 can provide prolonged endothelial protection during ischemia/reperfusion. There were no further differences in dextran diffusion rate amongst OGD control and treatment groups during 4-24h of ischemia/reperfusion (**Fig. 11f** and **S11b**).

3.10.2. Paracellular permeability of 4.4 kD TRITC-Dextran (a small molecule tracer) in PEG-DET/HSP27 and EV/HSP27 pre-treated HBMEC culture inserts

We measured the paracellular permeability of 4.4 kD TRITC-Dextran across HBMEC monolayers to evaluate the effect of PEG-DET/HSP27 and EV/HSP27 pre-treatment on the paracellular permeability of small molecules in primary HBMECs during normoxic, ischemic, and ischemic/reperfusion conditions. HBMECs were treated at a dose of 2 µg/well HSP27 complexed with PEG-DET at 20:1 w/w ratio and EXOs, MVs, EVs (EXO: MV=1:1) at 10:1 w/w ratio. Native HSP27, free PEG-DET, and naïve EXOs, MVs, and EVs were used as controls. The difference in the diffusion rate of 4.4 kD dextran between untreated and HSP27 complexes-treated cells during normoxic conditions and pre-OGD phase was not statistically significant ($p>0.05$) with the exceptions of MV/HSP27- and EV-treated groups (**Fig. 12a**). During the OGD phase, PEG-DET/HSP27, and (PEG-DET/HSP27)/EV-treated HBMECs showed a significant ($p<0.05$) reduction in the rates of 4.4 kD dextran diffusion compared to OGD, native HSP27, and free PEG-DET-treated HBMECs for 4 h (**Fig. 12b**). Besides, naïve EXO, MV, and EV-treated HBMECs showed a significant ($p<0.05$) reduction in paracellular permeability for 4 h (**Fig. 12b**) and 6 h (**Fig. 12c**) of OGD exposure. Interestingly, HBMECs exposed to EXO/HSP27, MV/HSP27, and EV/HSP27 did not affect the 4.4 kD dextran diffusion rate during 6 h of OGD.

(PEG-DET/HSP27)/EV, naïve EXOs, MVs, and EV/HSP27 mixtures showed a consistent and significant ($p<0.05$) reduction in the rate of 4.4 kD dextran diffusion for 24 h of OGD exposure (**Fig. S11c**).

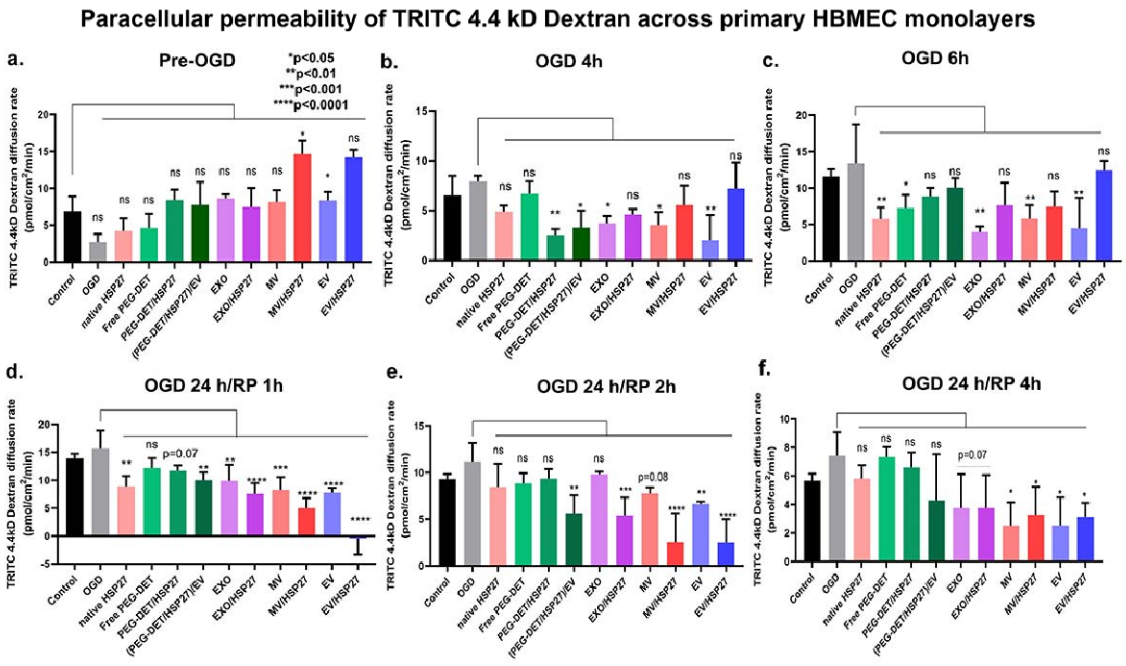

Fig. 12. Paracellular permeability of TRITC 4.4 kD Dextran under pre-OGD, OGD, and OGD/reperfusion conditions in HBMEC transwell culture inserts pre-treated with PEG-DET/HSP27 and EV/HSP27. HBMECs were seeded in 24-well plates and maintained in a 37°C humidified incubator for a week. The complete growth medium was replaced with 300 µL of growth media containing indicated treatment groups for 72 h. Post-incubation, the media was replaced with complete growth medium containing 1µM TRITC 4.4 kD Dextran for 1 h (Pre-OGD) **a**). Post-treatment, the treatment media was replaced with 300 µL of OGD medium containing 1 µM TRITC 4.4 kD Dextran for 24 h. The abluminal chamber was filled with 0.5 mL of complete growth medium. Control, untreated cells were incubated in complete growth medium in a humidified incubator whereas OGD treatment groups were incubated in an OGD chamber. At 4 (**b**) and 6 h post-OGD (**c**), a 500 µL volume was collected from the abluminal chamber and fresh medium was added to the transwell inserts. Post-OGD treatment, HBMECs were washed with PBS and incubated with 300 µL of complete growth medium containing 1µM TRITC 4.4 kD Dextran and incubated in a humidified incubator for 1-24h. At each time point, a 500 µL volume was collected from the abluminal chamber and fresh medium was added to the transwell inserts. The concentration of TRITC 4.4 kD Dextran was measured at 1 h (OGD/RP 1h, **d**), 2 h (OGD/RP 2h, **e**), and 4 h (OGD/RP 4h, **f**) using a Synergy HTX multimode plate reader at 485/20 nm excitation and 580/50 nm emission settings. The diffusion rate of TRITC 4.4 kD Dextran at each time point was calculated by normalizing the amount of TRITC Dextran per unit surface area of the insert per unit time. Data represent mean±SD (n=2). * p<0.05, ** p<0.01, *** p<0.001, **** p<0.0001, ns: non-significant.

1030

1031

1032

During the first hour of ischemia/reperfusion (OGD/RP), HBMECs exposed to native HSP27 and PEG-DET/HSP27 complexes showed a significant ($p<0.05$) reduction in 4.4 kD dextran diffusion rate compared to OGD and free PEG-DET polymer-treated cells (**Fig. 12d**). In addition, naïve EXOs, EVs, EXO/HSP27, MV/HSP27, and EV/HSP27 pre-treated HBMECs showed a highly significant ($p<0.0001$) decrease in 4.4 kD dextran diffusion rate compared to control OGD/RP HBMECs (**Fig. 12d**). MV/HSP27 and EV/HSP27-treatment mediated reduction in 4.4 kDa dextran diffusion rate was observed till 2 h of OGD/RP while the dextran diffusion rate in other treatment groups was non-significant compared to the untreated cells (**Fig. 12e**). There was no significant difference in dextran diffusion rate between control and treated OGD/RP HBMECs from 4 - 24 h (**Fig. 12f** and **S11d**). The possible reason for the observed lack of changes in the small molecule/4.4 kDa dextran diffusion rate during the reperfusion phase is likely due to the reperfusion-mediated rapid recovery of ischemic HBMECs.

4. Discussion

The lack of blood supply in brain blood vessels during ischemic stroke induces oxygen-glucose deprivation in brain tissues that results in sudden energy failure, mitochondrial damage, and disruption of BBB tight junctions in brain endothelial cells (2, 4). The restoration of blood flow/"ischemia/reperfusion" further damages the BBB integrity leads to increased paracellular permeability of toxins and immune cells from blood to the brain parenchyma (7, 43-45). The damage to the BBB-forming endothelial cells during ischemia/reperfusion disrupts the structure and function of the neurovascular unit and results in secondary brain damage leading to hemorrhagic transformation, poor neurological outcomes, and long-term cognitive impairments (9, 45). A treatment strategy that preserves the structure and function of the BBB would limit the

infiltration of deleterious molecules across the BBB, and consequently reduce the progression of brain injury and improve neurological functions in stroke patients (9). Therefore, a one, two-punch strategy to increase brain endothelial cell bioenergetics and decrease endothelial paracellular permeability is a promising approach to ameliorate ischemia/reperfusion-induced BBB damage post-ischemic stroke.

We have used EVs: a natural nanocarrier, for this one, two-punch delivery strategy. EVs are known to incorporate mitochondrial components such as mitochondria, mitochondrial DNA, and proteins along with their inherent nucleic acid, lipids, and protein cargoes during their biogenesis (39, 46-48). On the other hand, endothelial overexpression of HSP27 in a transgenic mouse model of focal cerebral ischemia decreased mice brain infarct volume compared to neuronally-overexpressed HSP27 and placebo mice (9, 10, 49). Therefore, the goal of this study was to engineer EVs for the delivery of exogenous HSP27 protein. The one, two-punch strategy is to harness the innate EV mitochondrial load to increase endothelial bioenergetics and we hypothesized that HSP27 delivery to endothelial cells can reduce paracellular permeability in ischemic endothelial cells. We believe that this approach to protect the brain endothelial cells is a potent strategy to decrease the long-term damage and dysfunction to the neurovascular unit that is comprised of endothelial cells, neurons, astrocytes, pericytes and microglia. Protection of the neurovascular unit is increasingly recognized as a vital component (9, 10, 45) of novel stroke therapies.

The present study investigated (1) the naïve EV-mediated increase in mitochondrial function of recipient human brain endothelial cells under normoxic and ischemic conditions, and (2) the

efficiency of EVs and a synthetic cationic polymer, PEG-DET, to interact/complex with HSP27 and their effect to decrease BBB permeability in ischemic brain endothelial cells. The results of our studies demonstrated that polarized mitochondria from EVs, specifically from MVs, were transferred into and colocalized with the mitochondrial network of the recipient endothelial cells. As a result, EV-treated primary HBMECs demonstrated increased intracellular ATP levels and mitochondrial respiration during normoxic and hypoxic conditions. Besides, EVs and PEG-DET polymer formed nano-sized complexes with recombinant human HSP27 protein demonstrating nano carrier-based approaches to deliver therapeutic proteins to the BBB. Importantly, prophylactic treatment of EV/HSP27 mixtures and PEG-DET/HSP27 complexes significantly reduced ischemia-induced paracellular permeability of small and large tracer molecules across primary HBMEC monolayers *in vitro*.

Brain endothelial cells form the foremost layer of the blood-brain barrier (BBB) and they contain about two to five-fold greater mitochondrial content compared to non-BBB cells (50). Moreover, the membranes of brain microvascular endothelial cell-derived EVs contain BBB receptors such as transferrin and insulin that enable EVs to cross the BBB for the treatment of various neurovascular disorders (51-53). A greater mitochondrial load and their natural affinity for BBB targeting motivated us to isolate exosomes (EXOs) and microvesicles (MVs) from a human cerebral microvascular endothelial (hCMEC/D3) cell line in our studies. We used an established differential ultracentrifugation, the most commonly used EV isolation method (54), to isolate MVs and EXOs from the conditioned medium. Cell debris and apoptotic bodies were eliminated from the conditioned medium at low-centrifugal speeds (2000×g) followed by pelleting MVs and EXOs at 20,000 and 120,000×g centrifugal forces, respectively. Post-

ultracentrifugation and resuspension, EXOs and MVs showed their characteristic particle diameters (100-250 nm, **Fig. 1a-d**) that largely aligned with the previous reports (19, 28, 38, 55, 56). Anionic phospholipid components such as phosphatidylinositol, phosphatidylserine, and glycosylated lipid derivatives exert a net negative zeta potential on the EXOs and MV membranes (**Fig. 1e,f**) (48, 57). The broad polydispersity indices demonstrate the natural heterogeneity of both EV sub-populations. Similar to cells and other biomolecules, it is important to preserve EV physicochemical characteristics and biological activities during storage conditions which critically determine the scope of their therapeutic application. Jeyaram *et al.* showed that EVs isolated from biofluids such as blood, milk, urine, and conditioned medium preserved their physical and functional properties stored at -80°C compared to 4° and -20°C (58, 59). Moreover, freeze-thaw cycles at -20° and -80°C did not affect the stability of plasma exosome miRNA (60). Lorincz *et al*. reported that 28 days of storage at -20° and -80°C did not affect the particle numbers of neutrophilic granulocyte-derived EVs, but moderately shifted their particle diameter and antibacterial activity (61). In our studies, EXOs and MVs isolated from conditioned medium retained their particle diameters, dispersity indices, and zeta potential after three consecutive freeze-thaw cycles (samples were frozen at -20°C for 24 h and then were thawed at room temperature for 1 h, **Fig. 1a-f**).

The integrity of the EXO and MV membranes immediately post-isolation and post-frozen storage were determined using a calcein-AM-based flow cytometry analysis. Calcein AM permeates the EV membranes, and as a result, intact vesicular esterases hydrolyze the acetoxymethyl-moiety of calcein AM to the non-permeant fluorescent calcein (62). The lack of esterases in damaged vesicles cannot activate the calcein-AM, therefore, this strategy can be

utilized to differentiate intact vs. disrupted under a variety of conditions such as post- EV isolation, storage, freeze-thaw cycles, and at various osmolarities (62-64). Mitchell *et al.* confirmed that exosome integrity was not affected by salt concentration-induced osmolarity changes in urine specimens using the calcein AM assay (64). Kong *et al.* utilized the calcein AM method to investigate the impact of storage conditions and anti-coagulants on MV particle counts and sizes using flow cytometry (63). The authors reported that the particle counts of calcein-labeled MV significantly decreased at -80°C storage for one to four weeks, however, remained unaffected during 4°C storage for a week. Our analysis of calcein-labeled EVs indicated that freezing EXOs and MVs at -20°C and thawing them thrice did not affect their particle count and membrane integrity compared to freshly-isolated EVs (**Fig. 1j,k**). Overall, our study demonstrated that naïve EXOs and MVs-isolated from conditioned medium preserved their physical characteristics, and at least >90% of EVs maintained their membrane integrity during the -20°C storage.

We confirmed the presence of ATP5A as we did in our previous studies (19, 28), a subunit of mitochondrial adenosine triphosphate synthase complex (19, 65), in the hCMEC/D3 cell line-derived MVs using western blotting (**Fig. S12**). The mitochondrial ATP5A plays important role in mitochondrial ATP production via catalyzing the synthesis of ATP from ADP in the mitochondrial matrix during oxidative phosphorylation (66). A considerably higher ATP5A band density in hCMEC/D3-derived MVs compared to EXOs suggested that MVs contain a greater mitochondrial load compared to EXOs. Todkar *et al.* demonstrated that Optic Atrophy-1 and sorting nexin 9-dependent pathways play an important role in sorting mitochondrial proteins into EVs and prevented the incorporation of damage-associated molecular patterns into EVs (39).

Phinney *et al.* have demonstrated that mesenchymal stem cells-derived MVs, but not EXOs, contained depolarized mitochondria (38). As a pro-survival mechanism during physiological or oxidative stress-induced mitophagy, mitochondria align with the plasma membranes and extrude into arrestin domain-containing protein-1-mediated MVs which bud outwards directly from the plasma membrane (38). Besides, macrophage-derived EXOs showed the presence of CD9 (**Fig. S12**), a tetraspanin EXO biomarker associated with exosomal cargo selection, binding, and uptake of EXOs by target cells (67) suggesting the purity of isolated EXOs using the ultracentrifugation. We also noted the presence of CD9 in MVs derived from hCMEC/D3 cells. Glyceraldehyde 3-phosphate dehydrogenase (GAPDH, 37 kD) was used as an additional control demonstrating the presence of cytosolic components in EXOs and MVs (**Fig. S12**). EXOs contained greater GAPDH compared to MVs likely due to increased cytosolic component incorporation during its biogenesis. Hence, the incorporation of mitochondrial components in naïve MVs and EXOs may have the potential to increase cellular ATP levels in the recipient cells.

Mitochondria, the central metabolic hub of cells, are essential organelles especially in high metabolic rate organs such as the brain (68). Mitochondria regulate and are involved in critical cellular events such as the production of cellular energy by ATP synthesis, induction of apoptosis, cell reproduction, growth, and differentiation, calcium homeostasis, immune activation, and mitophagy (39, 68, 69). Therefore, it is essential to maintain the quantity and quality of mitochondria for cell survival and tissue homeostasis. Under physiological conditions, a notable spontaneous intercellular transfer of mitochondria occurs during tissue homeostasis and development (70). During stress-induced conditions like oxygen-glucose deprivation in ischemic

stroke, ATP depletion-induced calcium accumulation and glutamate excitotoxicity increase electron leakage in mitochondria followed by increased reactive oxygen species (ROS) generation (3, 4, 70). The rapid accumulation of ROS in mitochondria drastically depolarizes the mitochondrial membrane potential, and consequently, degrades damaged mitochondria (70). Cells cannot survive upon mitochondrial dysfunction-induced cellular energy deprivation, and hence, mitochondrial replacement via supplementation of exogenous mitochondria or mitochondrial components is an efficient way to revitalize exhausted cells in many CNS disorders including ischemic stroke (71). Our TEM analysis demonstrated that MVs, but not EXOs, showed the presence of one or five mitochondria per MV (**Fig. 2 f-h**). Mitochondria-rich MV morphology was consistent with published reports (38, 72). Numerous *in vitro*, pre-clinical, and clinical studies have demonstrated that mitochondria or mitochondrial components such as mtDNA, mitochondrial proteins were secreted into the extracellular milieu and transferred between CNS cells (38, 47, 73-77). For instance, mesenchymal stem cell-derived-MV transferred mitochondria into the recipient macrophages leading to increased cellular bioenergetics (38). Guescini *et al*. provided evidence that exosomes were released from glioblastoma and astrocytes transfer mtDNA from glioblastoma to astrocytes (78). Mitochondria in MVs-derived from lipopolysaccharide-stimulated monocytes released mitochondria and mitochondrial transfer-mediated proinflammatory responses were observed in the recipient endothelial cells (47).

We isolated EXOs and MVs from the conditioned medium of Mitotracker deep red (MitoT-red) pre-stained hCMEC/D3 cells to label polarized mitochondria in EVs. MitoT-red is a mitochondrion membrane potential-dependent carbocyanine dye that selectively stains polarized mitochondria, and its fluorescence intensity is reduced during mitochondrial depolarization (79,

80). We demonstrated that MVs contain a greater polarized mitochondrial load compared to EXOs and efficiently transfer mitochondria into recipient human brain endothelial cells (**Fig. 3a-c, 4 and Fig. S4**). MV-associated mitochondria were transferred into the recipient endothelial cells within 24 h of incubation. Increasing the MV dose and incubation time significantly increased mitochondrial transfer in the recipient cells. Importantly, the transferred mitochondria efficiently integrated with the mitochondria network of recipient cells likely due to mitochondrial fusion. The colocalization of EV mitochondria and recipient cell mitochondria was confirmed by the presence of overlapping signals of the EV-mitochondria fluorescence signals with the recipient mitochondrial signals. We used two orthogonal approaches to stain the mitochondrial network in the recipient cells: Mitotracker green and the CellLight mitochondria-GFP BacMam technique (**Fig. 5, 6 and Fig. S6, 7**). The carbocyanine Mitotracker green dye stains the functional mitochondria in the recipient endothelial cells whereas CellLight Mitochondria-GFP BacMam comprising a fusion construct of α-pyruvate dehydrogenase and emGFP packaged in the baculoviral vector stains a structural mitochondrial matrix protein (α-pyruvate dehydrogenase) in the recipient cells (40). Thus, utilizing two orthogonal types of staining techniques, we demonstrated an efficient colocalization of polarized EV mitochondria with the polarized mitochondria in the recipient cells (via Mito-T-green staining, **Fig. 5**) and integration of functional, polarized EV mitochondria with the structurally intact mitochondria in the recipient cells (via CellLight Mitochondria-GFP staining, **Fig. 6**).

MVs and EXOs showed a dose-dependent increase in colocalization at 72 h, specifically, the MV mitochondria demonstrated a significantly greater colocalization coefficient compared to EXOs (**Fig. S5**). A selective mitochondrial packaging into endothelial cell-derived microvesicles

compared to exosomes was consistent with published reports (38, 47, 78). The uptake of the heterogenous EVs population by recipient cells depends on the membrane proteins and glycoproteins found on the surface of both the target cell and the EVs (81). Many studies have revealed that EVs can be endocytosed by different cells via different mechanisms including clathrin-mediated endocytosis (82, 83), caveolin-mediated endocytosis, endocytosis via lipid rafts, macropinocytosis (82), and phagocytosis (68, 81, 84, 85). The EV content is released to the receptor cells by direct fusion to the plasma membrane and they either unload their contents into the cytosol (86, 87), internalize with organelles such as endoplasmic reticulum, mitochondria (88), and nucleus (89), or be routed to the lysosomes for degradation. Conqvist *et al.* have shown that EVs derived from placental syncytiotrophoblast internalized into primary endothelial cells via clathrin-mediated endocytosis and transferred placenta-specific miRNA from EVs into the endoplasmic reticulum and mitochondria of the recipient cells (83, 88). Islam *et al*. reported that bone-marrow-stromal cell-derived mitochondria-containing MVs donated functional mitochondria to alveolar epithelial cells via connexin 43-containing gap junction channels (74). Phinney *et al.* showed that MVs mitochondria fused with recipient macrophages to unload partially depolarized mitochondria, thereby increasing the recipient cell's bioenergetics (38). Overall, MV-mediated transfer of functional mitochondria and their colocalization with recipient endothelial mitochondrial network resulted in the mitochondrial transfer-mediated increases in cellular ATP levels and mitochondrial respiration under normoxic and ischemic conditions.

One of the main functions of mitochondria is to synthesize ATP from ADP during mitochondrial aerobic respiration, and therefore, we measured the resulting relative ATP levels in the recipient endothelial cells treated with EXOs or MVs using a Cell Glo ATP assay. The

Cell Titer Glo reagent lyses the cells resulting in the release of intracellular ATP that activates the conversion of luciferin to luciferase. This sensitive, rapid, and reproducible cell viability assay is directly proportional to the amount of ATP in metabolically viable cells (90). Our results demonstrated that naïve EXOs and MVs showed a dose-dependent significant increase in the relative ATP levels at 48 h-post incubation (**Fig. 7a-c**). Importantly, MVs outperformed EXOs in increasing recipient cell viability and the effects persisted for 72 h-post incubation (**Fig. 7b,c**). Islam *et al*. reported that mitochondria containing MVs derived from bone marrow stromal cells increased ATP levels of alveolar epithelial cells (74). Guo *et al*. demonstrated that transfer of mitochondria isolated from donor bone marrow-derived mesenchymal cells (BMSC) into the recipient BMSCs increased cellular ATP production, proliferation, migration, and repaired bone defects *in vitro* and *in vivo* (91).

Ischemia-induced oxygen-glucose deprivation leads to a sudden drop in the endothelial ATP levels cells that subsequently switch off the Na^+/K^+ and Ca^{2+} ATPase ionic transporters (2-4). The sodium and calcium accumulation in endothelial cells potentiate endothelial cell death through glutamate and dopamine excitotoxicity coupled with cellular depolarization. Numerous cell culture, preclinical, and clinical studies have demonstrated the ischemia-induced cerebral endothelial dysfunction/apoptosis and BBB breakdown (92-95). In our studies, endothelial cells exposed to oxygen-glucose deprived (OGD) exposure in a hypoxic chamber led to about 40% at 4 h and 60% endothelial cell death at 24 h compared to untreated cells (**Fig. 7d**). The observed data is consistent with the published reports (96, 97). Our results showed that primary HBMECs treated with hCMEC/D3-derived naïve EXOs and MVs resulted in a four to five-fold increase in endothelial ATP levels compared to control, untreated cells (**Fig. 7e**). Importantly, EV-mediated

increases in ATP levels were dose-dependent and MVs outperformed compared to EXOs in rescuing the ATP levels and consequently the survival of ischemic primary HBMECs 24 h post-OGD (**Fig. 7e**). It can be inferred from our western blot results and published reports (38, 39) that the MV-mediated increase in recipient endothelial cell ATP levels is associated with the presence of functional mitochondria and mitochondrial proteins and their transfer into the recipient cells. High throughput proteomic analysis revealed 89 types of mitochondrial proteins in MVs vs. a single type in EXOs isolated from hCMEC/D3 cells (32). The presence of mitochondrial components such as mtDNA and mitochondrial proteins in EXOs can also enhance cellular mitochondrial function (32, 55). A published report has shown that EXOs isolated from healthy and asthmatic human airway myeloid-derived regulatory cells incorporated mitochondria that transferred and colocalized with the mitochondria of recipient T cells (32). Kong *et al.* reported that treatment with mesenchymal stem cell (MSC)-derived exosomes rescued OGD-induced rat primary brain endothelial cell death (98). Arslan *et al.* reported that MSC-derived exosomes resulted in a two-fold increase in ATP levels in ischemia/reperfused mice compared to saline (99). The authors reported that administration of EXOs five minutes prior to reperfusion in ischemic mice showed about a 45% decrease in mice myocardium infarct volume compared to saline treatment. Besides, murine hemibrain-isolated EVs containing mitovesicles showed a two-fold increase in brain ATP levels compared to oligomycin and antimycin-I treated EVs (100). Overall, MV-associated mitochondria and exosomal mtDNA and/or mitochondrial proteins have shown the potential to rescue normoxic and ischemic endothelial cells in a dose- and time-dependent manner by increasing intracellular ATP levels.

Metabolic pathways such as mitochondrial respiration and glycolysis are the major sources of ATP for cellular energy production (101). Therefore, we investigated the effects of MV and EXO treatment on mitochondrial respiration and glycolytic capacity function in the recipient endothelial cells using a Seahorse setup. The state-of-art Seahorse extracellular flux (XF) analyzer allows measuring the extracellular acidification rate (ECAR), an indicator of glycolysis, and the oxygen consumption rates (OCR), an indicator of mitochondrial respiration in real-time in live intact cells (102, 103). Glycolysis takes place in the cytosol where a series of metabolic reactions converts glucose into pyruvate followed by reversible formation of lactate and hydrogen ions which release into the extracellular spaces. Glycolysis is an oxygen-independent process that generates two ATP molecules from a single glucose molecule (104). On the other hand, mitochondrial respiration involves electron transport and oxidative phosphorylation that takes place in the inner mitochondrial membrane and generates 34 ATP molecules per cycle of the electron transport chain (105). During oxidative phosphorylation, tricyclic acid pathway-derived electrons combine with oxygen, and the energy resulting from this redox reaction drives the synthesis of ATP from ADP (105).

We demonstrated that hCMEC/D3 cells treated with EXOs and MVs show a dose-dependent significant increase in basal and maximum OCR at 72 h exposure (**Fig. 8a-c**). Consistent with ATP assays (**Fig. 7a-c**), the MV-mediated increase in maximum mitochondrial respiration was greater than EXOs suggesting that MV mitochondria efficiently increased the recipient cell mitochondrial function under physiological/normoxic conditions. Interestingly, we noted that EXOs showed a dose-dependent and significantly greater increase in recipient glycolysis capacity compared to MVs. We speculate that MVs likely colocalize with the mitochondria

whereas EXOs are released into the cytosol and thereby contribute to the greater glycolytic capacity. Phinney *et al.* demonstrated that MSC-derived EXOs and MVs significantly increased basal and maximum OCR in the recipient macrophages compared to controls in MSC-macrophage cocultures (38). Published reports have indicated that the transfer of only a few mitochondria, even partially depolarized mitochondria is sufficient to rescue cellular bioenergetics in mtDNA-depleted recipient cells (38, 73, 106). Overall, our western blotting results (**Fig. S12**) and Mitotracker deep red staining studies (**Fig. 4**) confirmed the presence of mitochondrial proteins and functional mitochondria in EVs. MV mitochondria-mediated increase in recipient cellular mitochondrial respiration at 72 h (**Fig. 8**) is likely explained by the greater transfer and colocalization of MitoT-red-MVs (**Fig. 4-6, S5,6**) into primary human brain endothelial cells and the greater extent of increases in intracellular ATP (**Fig. 7a-c**). Our use of these orthogonal tools and observations demonstrate that MVs carry a higher load of functional mitochondria compared to EXOs. The maximum transfer and colocalization of MV mitochondria within the recipient primary human brain endothelial cells take about 48 to 72 h and this mitochondrial uptake consequently results in increased cellular ATP levels, mitochondrial respiration, and glycolytic capacities.

BBB breakdown is one of the hallmarks of ischemic stroke pathology, which is initiated due to hypoperfusion-induced oxygen-glucose deprivation and persists for several days to weeks even after the restoration of blood flow (ischemia/reperfusion) (2-4). Following the onset of ischemic stroke, alteration and endocytosis of BBB-forming tight and adherens junction proteins cause increased leakage of paracellular solutes and immune cells from blood to the brain parenchyma (3). Under physiological/normoxic conditions, tight junction proteins and adhesion

proteins associate with accessory proteins such as zonula occludens-1 (ZO-1) that are further anchored to cytoskeleton proteins such as α-actin (9, 107). Independent of the metalloproteinase-mediated degradation of endothelial tight junctions, ischemia/reperfusion induces rapid actin polymerization in endothelial cells resulting in the formation of stress fibers consisting of F-actin, myosin, and other proteins (9, 45). The transmission of this intracellular tension results in the disassembly of the actin cytoskeleton leading to the internalization of tight junction and adherens junction proteins in endothelial cells. Shi *et al.* demonstrated that endothelial overexpression of HSP27 in transgenic mice showed a significant and prolonged reduction in infarct volume compared to neuronal overexpression of HSP27 and saline-treated transgenic focal ischemic mice (9). HSP27 inhibits the actin polymerization, therefore, reduces the G-actin/F-actin ratio consequently restores the tight junction integrity and enhances BBB protection during ischemia/reperfusion (9, 10). Therefore, we delivered HSP27 into primary brain endothelial cells to determine the HSP27-mediated protection of paracellular permeability across the endothelial monolayers. Native HSP27 has a half-life of about 2 h (108) and is susceptible to protease and enzymatic degradation in plasma and physiological conditions (109).

We used EVs as a natural nanocarrier and PEG-DET as a synthetic carrier to deliver HSP27 into endothelial cells. The isoelectric point of human recombinant HSP27 is 5.89 (42), therefore, it exerts a net negative charge at physiological pH 7.4 (**Fig. 10a**). Diethyltriamine side chain of PEG-DET cationic diblock copolymer has two pKa values associated with its molecular conformation (*gauche vs. anti*). The *gauche* conformation of DET exerts a pKa of 9.9 that induces the formation of stable complexes with negatively charged nucleotides at physiological pH 7.4 (24, 110). We confirmed the formation of PEG-DET/HSP27 complexes using native

PAGE followed by Coomassie staining (**Fig. 9a,b**) and dynamic light scattering (**Fig. 10a-c**). The optimal PEG-DET/HSP27 w/w ratio of 20/1 formed a complex with about 70% of HSP27 incorporation which was further confirmed by the disappearance of the HSP27 band in native PAGE (**Fig. 9a**) and a shift in the zeta potential from ca. -9 mV (HSP27) to about +9 mV (PEG-DET/HSP27 complexes) (**Fig. 10c**). These nano-sized complexes showed unimodal and narrow particle size distribution further confirming the formation of complexes in the solution.

Despite the negative surface charge of EVs and the native HSP27 protein at pH 7.4, hCMEC/D3-EV/HSP27 mixtures showed about 20% protein interaction in native PAGE analysis without affecting the physicochemical characteristics of naïve EVs. Haney *et al*. also reported that macrophage-derived exosomes incubated with bovine liver catalase proteins did not affect the particle diameter and dispersity indices of the EXO/catalase mixture (111). Notably, the zeta potential of EV/HSP27 mixtures was significantly different compared to native HSP27. It is possible that native HSP27 passively diffuses into the EV lumen as well as forms weak protein-protein hydrophobic interactions (112) or the mixtures may be stabilized by nonbonded interactions such as H-H bonds. The weaker interactions of HSP27 with EVs were advantageous for our study as we wanted to avoid any mode of intrusive cargo loading (such as sonication, freeze/thaw cycles, saponin-mediated loading) that may damage the integrity of EV membranes and inversely impact the functionality of innate cargoes, specifically, their mitochondrial load. We further confirmed the MV and HSP27 interactions using an immunoprecipitation pull-down assay (**Fig. S13**). We engineered ternary mixtures of EVs with PEG-DET/HSP27 complexes at different weight ratios to increase the HSP27 loading into hCMEC/D3-derived EVs. The positively-charged PEG-DET/HSP27 complexes (+9 mV, **Fig. 10c**) formed an electrostatic

complex with EXOs and MVs which was confirmed by an intermediate HSP7 band density between PEG-DET/HSP27 complexes and EXO/HSP27 mixtures (**Fig. 9h**) and increased resulting particle diameters (**Fig. 10d**). (PEG-DET/HSP27)/EV complexes showed an electroneutral or slight-positive zeta potential (**Fig. 10f**) which may allow longer systemic circulation and a greater cellular uptake. The inclusion of EVs in (PEG-DET/HSP27)/EV complexes may facilitate interactions with the BBB and mediate endothelial targeting (113) during *in vivo* delivery while the positive charges derived from PEG-DET can enhance the cellular uptake and facilitate endosomal escape of HSP27 (24). The cytosolic release of HSP27 in endothelial cells can and reduce paracellular permeability of hydrophilic molecules and immune cells (9) and ultimately increase the BBB integrity.

We evaluated the prophylactic PEG-DET/HSP27 and EV/HSP27 treatment-induced protection of BBB integrity by measuring the diffusion rate of the hydrophilic tracers varying in molecular mass across cultured endothelial monolayers under ischemia/reperfusion conditions. The diffusion rate of the larger 65-85 kD TRITC-Dextran in untreated hCMEC/D3 cells and HBMECs were compared at pre-OGD conditions, during OGD, and OGD/reperfusion conditions (**Fig. S14**). The baseline diffusion rate was found to be different for both cell models. The diffusion rate gradually increased and was relatively higher for the hCMEC/D3 cell line compared to the HBMEC monolayer during ischemia/reperfusion (RP) suggesting the inherent leakiness of the hCMEC/D3 cell line compared to primary HBMECs. Therefore, we studied the effects of naïve EV and HSP27 complexes exposure on the diffusion rate of 4.4 kD and 65-85 kD TRITC-dextran during OGD and OGD/RP conditions in primary HBMEC monolayers. Naïve EVs, PEG-DET/HSP27, and EV/HSP27 complexes were cytocompatible with HBMECs

for 72 h of exposure under normoxic conditions (**Fig. 7f**). Notably, EXO/HSP27, MV/HSP27, and EV/HSP27 mixtures significantly increased cell viability compared to untreated cells and are likely an additive effect of naïve EV mitochondrial transfer and anti-apoptotic/cell proliferation effects of HSP27 (114-117).

First, we analyzed the effect of exposure of naïve EV, PEG-DET/HSP27 complexes, and EV/HSP27 mixtures on the diffusion rate of 65-85 kD TRITC-Dextran, a large molecular weight tracer simulating the infiltration of proteins and blood-borne large molecules during ischemia/reperfusion. Exposure of different treatment groups for 72 h did not affect the baseline permeability of HBMECs for large molecules, importantly, EXO/HSP27 mixtures showed an added effect on limiting diffusion of the TRITC-Dextran (**Fig. 11a**). Interestingly, HBMECs treated with PEG-DET/HSP27 complexes efficiently decreased 65-85 kD TRITC-Dextran diffusion rate for 6 h of OGD exposure followed by an immediate hour of ischemia/reperfusion compared to OGD-HBMEC control, native HSP27, and free PEG-DET-treated groups (**Fig. 11b-f**). These results indicated that PEG-DET-mediated efficient transfer of HSP27 in endothelial cells could restore the integrity of tight junctions and protect BBB integrity during ischemia and ischemia/reperfusion injury. Importantly, naïve EXO and MV-treated HBMECs showed strong BBB protection during OGD conditions and the first hour of ischemia/reperfusion. It should be noted that naïve EXOs also contain HSP proteins such as HSP20, HSP27, HSP40, and HSP70 (118-121), and therefore, the innate HSP load in EXOs and MV mitochondria could enhance overall endothelial cell survival and tight junction integrity during OGD conditions. EV/HSP27 mixtures further strengthened the BBB tight junction demonstrating that EV facilitates HSP27 transfer into endothelial cells resulting in synergistic BBB protection from large molecule

infiltration during ischemia and ischemia/reperfusion injury. We inferred that the integrity of tight junction proteins was restored after 2 h of reperfusion due to a similar dextran diffusion rate in OGD, control, and treatment groups. Therefore, it is essential to protect endothelial tight junction integrity during the early stage of ischemia/reperfusion (<2 h in culture conditions). Importantly, PEG-DET/HSP27, EV/HSP27, and naïve EV-mediated immediate BBB protection during the early reperfusion stage demonstrate their promising role in ischemic stroke therapy. Lastly, we further confirmed the naïve EV, PEG-DET/HSP27, and EV/HSP27-induced protection of BBB from the paracellular flux of small molecules under OGD and OGD/RP conditions. PEG-DET/HSP27 complexes strengthened the tight junctions to restrict 4.4 kD dextran entry up until 4 h of OGD exposure and an immediate hour of OGD/RP (**Fig. 12a-f**). Importantly, naïve EVs, but not their HSP27 complexes, retarded small molecule permeability during OGD conditions. Furthermore, naïve EV and their HSP27 complexes reduced 4.4 kD dextran diffusion for 6 h of ischemia/reperfusion injury. Notably, the magnitude of EV/HSP27 complex-mediated BBB protection is considerably greater than naïve EVs demonstrating a synergistic effect of EVs and HSP27 in increasing endothelial tight junction integrity. Noteworthy, naïve EV and EV/HSP27 complexes-mediated reduction in 4.4 kD and 65-85 kD dextran diffusion rate were significantly higher and prolonged compared to polymer-based HSP27 delivery (**Fig. 11,12**).

To summarize, endothelial cell-derived naïve MVs and EXOs contain functional mitochondria and mitochondrial proteins that internalize and integrate with the mitochondrial network of recipient endothelial cells. As a result, naïve MVs and EXOs increased ATP levels, mitochondrial respiration, and glycolytic capacities in the recipient brain endothelial cells. EXOs

and MVs form non-bonded interactions with exogenous therapeutic HSP27 protein and HSP27 delivery resulted in increased tight junction integrity in primary human brain endothelial cells by limiting the paracellular permeability of small and large molar mass tracer molecules during ischemia/reperfusion injury.

5. Conclusion

This one, two-punch approach increased the brain endothelial cell survival and their mitochondrial function due to the innate EV mitochondrial load, and EV/HSP27 restored BBB tight junction integrity by limiting the paracellular permeability of small and large molecular mass tracers. The outcome of the present study indicates that this approach has a strong potential to protect the BBB that in turn can ameliorate the long-term neurological damage and dysfunction in *in vivo* models of ischemic stroke.

Acknowledgments

This work was supported via start-up funds for the Manickam laboratory from Duquesne University (DU) and a 2021 Faculty Development Fund (Office of Research, DU) to the PI. We would like to acknowledge the Neurodegenerative Undergraduate Research Experience (NURE) R25NS100118 for funding DXD. The authors express their deep appreciation to Dr. Rehana Leak (DU) for her insights and technical advice. The authors are thankful to Dr. Lauren O'Donnell, and Mss. Manisha Chandwani and Yashika Kamte (DU) for flow cytometry support.

Author contribution

Conceptualization D.S.M **Experiment design** K.M.D and D.S.M **Seahorse studies** K.M.D, M.J.R, S.S.S, D.S.M **Transmission electron microscopy** K.M.D and D.B.S **PEG-DET synthesis** Y.B **EV physicochemical characterization** K.M.D, R.B, D.D, H.Y, R.R **Flow cytometry, Fluorescence microscopy, Permeability assays** K.M.D, D.S.M **Data analysis** K.M.D, D.S.M **Manuscript writing** K.M.D, D.S.M

References

1. https://www.cdc.gov/stroke/facts.htm
2. Nian K, Harding IC, Herman IM, Ebong EE. Blood-Brain Barrier Damage in Ischemic Stroke and Its Regulation by Endothelial Mechanotransduction. Front Physiol. 2020;11(1681).
3. Abdullahi W, Tripathi D, Ronaldson PT. Blood-brain barrier dysfunction in ischemic stroke: targeting tight junctions and transporters for vascular protection. Am J Physiol Cell Physiol. 2018;315(3):C343-C56.
4. Bernardo-Castro S, Sousa JA, Brás A, Cecília C, Rodrigues B, Almendra L, et al. Pathophysiology of Blood–Brain Barrier Permeability Throughout the Different Stages of Ischemic Stroke and Its Implication on Hemorrhagic Transformation and Recovery. Frontiers in Neurology. 2020;11(1605).
5. Liu S, Feng X, Jin R, Li G. Tissue plasminogen activator-based nanothrombolysis for ischemic stroke. Expert Opin Drug Deliv. 2018;15(2):173-84.
6. Zhang Y, Wang Y, Zuo Z, Wang Z, Roy J, Hou Q, et al. Effects of tissue plasminogen activator timing on blood-brain barrier permeability and hemorrhagic transformation in rats with transient ischemic stroke. J Neurol Sci. 2014;347(1-2):148-54.
7. Jiang X, Andjelkovic AV, Zhu L, Yang T, Bennett MVL, Chen J, et al. Blood-brain barrier dysfunction and recovery after ischemic stroke. Prog Neurobiol. 2018;163-164:144-71.
8. Stamatovic SM, Keep RF, Wang MM, Jankovic I, Andjelkovic AV. Caveolae-mediated internalization of occludin and claudin-5 during CCL2-induced tight junction remodeling in brain endothelial cells. J Biol Chem. 2009;284(28):19053-66.
9. Shi Y, Jiang X, Zhang L, Pu H, Hu X, Zhang W, et al. Endothelium-targeted overexpression of heat shock protein 27 ameliorates blood-brain barrier disruption after ischemic brain injury. Proc Natl Acad Sci U S A. 2017;114(7):E1243-e52.
10. Leak RK, Zhang L, Stetler RA, Weng Z, Li P, Atkins GB, et al. HSP27 protects the blood-brain barrier against ischemia-induced loss of integrity. CNS Neurol Disord Drug Targets. 2013;12(3):325-37.
11. Rada CC, Mejia-Pena H, Grimsey NJ, Cordova IC, Olson J, Wozniak JM, et al. Heat shock protein 27 activity is linked to endothelial barrier recovery after proinflammatory GPCR-induced disruption. Sci Signal. 2021;14(698):eabc1044.
12. During RL, Gibson BG, Li W, Bishai EA, Sidhu GS, Landry J, et al. Anthrax lethal toxin paralyzes actin-based motility by blocking Hsp27 phosphorylation. EMBO J. 2007;26(9):2240-50.

13. Hirano S, Rees RS, Yancy SL, Welsh MJ, Remick DG, Yamada T, et al. Endothelial barrier dysfunction caused by LPS correlates with phosphorylation of HSP27 in vivo. Cell Biol Toxicol. 2004;20(1):1-14.
14. Miron T, Vancompernolle K, Vandekerckhove J, Wilchek M, Geiger B. A 25-kD inhibitor of actin polymerization is a low molecular mass heat shock protein. J Cell Biol. 1991;114(2):255-61.
15. Jakob U, Gaestel M, Engel K, Buchner J. Small heat shock proteins are molecular chaperones. J Biol Chem. 1993;268(3):1517-20.
16. Garrido C, Bruey JM, Fromentin A, Hammann A, Arrigo AP, Solary E. HSP27 inhibits cytochrome c-dependent activation of procaspase-9. FASEB J. 1999;13(14):2061-70.
17. Voss OH, Batra S, Kolattukudy SJ, Gonzalez-Mejia ME, Smith JB, Doseff AI. Binding of caspase-3 prodomain to heat shock protein 27 regulates monocyte apoptosis by inhibiting caspase-3 proteolytic activation. J Biol Chem. 2007;282(34):25088-99.
18. Bruey JM, Ducasse C, Bonniaud P, Ravagnan L, Susin SA, Diaz-Latoud C, et al. Hsp27 negatively regulates cell death by interacting with cytochrome c. Nat Cell Biol. 2000;2(9):645-52.
19. D'Souza A, Burch A, Dave KM, Sreeram A, Reynolds MJ, Dobbins DX, et al. Microvesicles transfer mitochondria and increase mitochondrial function in brain endothelial cells. J Control Release. 2021;338:505-26.
20. Banks WA, Sharma P, Bullock KM, Hansen KM, Ludwig N, Whiteside TL. Transport of Extracellular Vesicles across the Blood-Brain Barrier: Brain Pharmacokinetics and Effects of Inflammation. International journal of molecular sciences. 2020;21(12):4407.
21. Murphy DE, de Jong OG, Brouwer M, Wood MJ, Lavieu G, Schiffelers RM, et al. Extracellular vesicle-based therapeutics: natural versus engineered targeting and trafficking. Experimental & Molecular Medicine. 2019;51(3):1-12.
22. Doyle LM, Wang MZ. Overview of Extracellular Vesicles, Their Origin, Composition, Purpose, and Methods for Exosome Isolation and Analysis. Cells. 2019;8(7):727.
23. He Z, Ning N, Zhou Q, Khoshnam SE, Farzaneh M. Mitochondria as a therapeutic target for ischemic stroke. Free Radical Biology and Medicine. 2020;146:45-58.
24. Jiang Y, Arounleut P, Rheiner S, Bae Y, Kabanov AV, Milligan C, et al. SOD1 nanozyme with reduced toxicity and MPS accumulation. J Control Release. 2016;231:38-49.
25. Han M, Bae Y, Nishiyama N, Miyata K, Oba M, Kataoka K. Transfection study using multicellular tumor spheroids for screening non-viral polymeric gene vectors with low cytotoxicity and high transfection efficiencies. Journal of Controlled Release. 2007;121(1):38-48.
26. Xiong MP, Bae Y, Fukushima S, Forrest ML, Nishiyama N, Kataoka K, et al. pH-Responsive Multi-PEGylated Dual Cationic Nanoparticles Enable Charge Modulations for Safe Gene Delivery. ChemMedChem. 2007;2(9):1321-7.
27. Lai TC, Bae Y, Yoshida T, Kataoka K, Kwon GS. pH-Sensitive Multi-PEGylated Block Copolymer as a Bioresponsive pDNA Delivery Vector. Pharmaceutical Research. 2010;27(11):2260-73.
28. Dave KM, Zhao W, Hoover C, D'Souza A, S Manickam D. Extracellular Vesicles Derived from a Human Brain Endothelial Cell Line Increase Cellular ATP Levels. AAPS PharmSciTech. 2021;22(1):18.
29. Chen TH, Bae Y, Furgeson DY, Kwon GS. Biodegradable hybrid recombinant block copolymers for non-viral gene transfection. Int J Pharm. 2012;427(1):105-12.

30. Kanayama N, Fukushima S, Nishiyama N, Itaka K, Jang W-D, Miyata K, et al. A PEG-Based Biocompatible Block Catiomer with High Buffering Capacity for the Construction of Polyplex Micelles Showing Efficient Gene Transfer toward Primary Cells. ChemMedChem. 2006;1(4):439-44.
31. Donker RB, Mouillet JF, Chu T, Hubel CA, Stolz DB, Morelli AE, et al. The expression profile of C19MC microRNAs in primary human trophoblast cells and exosomes. Mol Hum Reprod. 2012;18(8):417-24.
32. Hough KP, Trevor JL, Strenkowski JG, Wang Y, Chacko BK, Tousif S, et al. Exosomal transfer of mitochondria from airway myeloid-derived regulatory cells to T cells. Redox Biol. 2018;18(2213-2317):54-64.
33. Dave KM, Ali L, Manickam DS. Characterization of the SIM-A9 cell line as a model of activated microglia in the context of neuropathic pain. PLOS ONE. 2020;15(4):e0231597.
34. Dave KM, Han L, Jackson MA, Kadlecik L, Duvall CL, D SM. DNA Polyplexes of a Phosphorylcholine-Based Zwitterionic Polymer for Gene Delivery. Pharm Res. 2020;37(9):176.
35. Dai X, Chen J, Xu F, Zhao J, Cai W, Sun Z, et al. TGFalpha preserves oligodendrocyte lineage cells and improves white matter integrity after cerebral ischemia. J Cereb Blood Flow Metab. 2020;40(3):639-55.
36. Cardenes N, Corey C, Geary L, Jain S, Zharikov S, Barge S, et al. Platelet bioenergetic screen in sickle cell patients reveals mitochondrial complex V inhibition, which contributes to platelet activation. Blood. 2014;123(18):2864-72.
37. Anne Stetler R, Leak RK, Gao Y, Chen J. The dynamics of the mitochondrial organelle as a potential therapeutic target. Journal of cerebral blood flow and metabolism : official journal of the International Society of Cerebral Blood Flow and Metabolism. 2013;33(1):22-32.
38. Phinney DG, Di Giuseppe M, Njah J, Sala E, Shiva S, St Croix CM, et al. Mesenchymal stem cells use extracellular vesicles to outsource mitophagy and shuttle microRNAs. Nature Communications. 2015;6(1):8472.
39. Todkar K, Chikhi L, Desjardins V, El-Mortada F, Pépin G, Germain M. Selective packaging of mitochondrial proteins into extracellular vesicles prevents the release of mitochondrial DAMPs. Nature Communications. 2021;12(1):1971.
40. CellLight™ Mitochondria-GFP, BacMam 2.0 (ThermoFisher website)
41. https://www.agilent.com/en/products/cell-analysis/how-seahorse-xf-analyzers-work.
42. http://protcalc.sourceforge.net/.
43. Venkat P, Chopp M, Chen J. Blood-Brain Barrier Disruption, Vascular Impairment, and Ischemia/Reperfusion Damage in Diabetic Stroke. J Am Heart Assoc. 2017;6(6):e005819.
44. Arba F, Rinaldi C, Caimano D, Vit F, Busto G, Fainardi E. Blood-Brain Barrier Disruption and Hemorrhagic Transformation in Acute Ischemic Stroke: Systematic Review and Meta-Analysis. Front Neurol. 2020;11:594613.
45. Shi Y, Zhang L, Pu H, Mao L, Hu X, Jiang X, et al. Rapid endothelial cytoskeletal reorganization enables early blood–brain barrier disruption and long-term ischaemic reperfusion brain injury. Nature Communications. 2016;7(1):10523.
46. Falchi AM, Sogos V, Saba F, Piras M, Congiu T, Piludu M. Astrocytes shed large membrane vesicles that contain mitochondria, lipid droplets and ATP. Histochem Cell Biol. 2013;139(2):221-31.
47. Puhm F, Afonyushkin T, Resch U, Obermayer G, Rohde M, Penz T, et al. Mitochondria Are a Subset of Extracellular Vesicles Released by Activated Monocytes and Induce Type I IFN and TNF Responses in Endothelial Cells. Circulation Research. 2019;125(1):43-52.

48. El Andaloussi S, Mäger I, Breakefield XO, Wood MJA. Extracellular vesicles: biology and emerging therapeutic opportunities. Nature Reviews Drug Discovery. 2013;12(5):347-57.
49. Shimada Y, Shimura H, Tanaka R, Yamashiro K, Koike M, Uchiyama Y, et al. Phosphorylated recombinant HSP27 protects the brain and attenuates blood-brain barrier disruption following stroke in mice receiving intravenous tissue-plasminogen activator. PLOS ONE. 2018;13(5):e0198039.
50. Oldendorf WH, Cornford ME, Brown WJ. The large apparent work capability of the blood-brain barrier: a study of the mitochondrial content of capillary endothelial cells in brain and other tissues of the rat. Ann Neurol. 1977;1(5):409-17.
51. Schiera G, Di Liegro CM, Di Liegro I. Extracellular Membrane Vesicles as Vehicles for Brain Cell-to-Cell Interactions in Physiological as well as Pathological Conditions. BioMed Research International. 2015;2015:152926.
52. Andras IE, Toborek M. Extracellular vesicles of the blood-brain barrier. Tissue Barriers. 2016;4(1):e1131804.
53. Yang T, Martin P, Fogarty B, Brown A, Schurman K, Phipps R, et al. Exosome delivered anticancer drugs across the blood-brain barrier for brain cancer therapy in Danio rerio. Pharm Res. 2015;32(6):2003-14.
54. Yang D, Zhang W, Zhang H, Zhang F, Chen L, Ma L, et al. Progress, opportunity, and perspective on exosome isolation - efforts for efficient exosome-based theranostics. Theranostics. 2020;10(8):3684-707.
55. Dozio V, Sanchez JC. Characterisation of extracellular vesicle-subsets derived from brain endothelial cells and analysis of their protein cargo modulation after TNF exposure. J Extracell Vesicles. 2017;6(1):1302705.
56. Kanada M, Bachmann MH, Hardy JW, Frimannson DO, Bronsart L, Wang A, et al. Differential fates of biomolecules delivered to target cells via extracellular vesicles. Proceedings of the National Academy of Sciences. 2015;112(12):E1433-E42.
57. Konoshenko MY, Lekchnov EA, Vlassov AV, Laktionov PP. Isolation of Extracellular Vesicles: General Methodologies and Latest Trends. Biomed Res Int. 2018;2018:8545347.
58. Jeyaram A, Jay SM. Preservation and Storage Stability of Extracellular Vesicles for Therapeutic Applications. AAPS J. 2017;20(1):1.
59. Ge Q, Zhou Y, Lu J, Bai Y, Xie X, Lu Z. miRNA in Plasma Exosome is Stable under Different Storage Conditions. Molecules. 2014;19(2):1568-75.
60. Witwer KW, Buzás EI, Bemis LT, Bora A, Lässer C, Lötvall J, et al. Standardization of sample collection, isolation and analysis methods in extracellular vesicle research. J Extracell Vesicles. 2013;2(1):20360.
61. Lőrincz ÁM, Timár CI, Marosvári KA, Veres DS, Otrokocsi L, Kittel Á, et al. Effect of storage on physical and functional properties of extracellular vesicles derived from neutrophilic granulocytes. J Extracell Vesicles. 2014;3(1):25465.
62. Gray WD, Mitchell AJ, Searles CD. An accurate, precise method for general labeling of extracellular vesicles. MethodsX. 2015;2:360-7.
63. Kong F, Zhang L, Wang H, Yuan G, Guo A, Li Q, et al. Impact of collection, isolation and storage methodology of circulating microvesicles on flow cytometric analysis. Exp Ther Med. 2015;10(6):2093-101.
64. Mitchell PJ, Welton J, Staffurth J, Court J, Mason MD, Tabi Z, et al. Can urinary exosomes act as treatment response markers in prostate cancer? J Transl Med. 2009;7:4.

65. Goldberg J, Currais A, Prior M, Fischer W, Chiruta C, Ratliff E, et al. The mitochondrial ATP synthase is a shared drug target for aging and dementia. Aging Cell. 2018;17(2):e12715.
66. Jonckheere AI, Smeitink JAM, Rodenburg RJT. Mitochondrial ATP synthase: architecture, function and pathology. J Inherit Metab Dis. 2012;35(2):211-25.
67. Andreu Z, Yáñez-Mó M. Tetraspanins in extracellular vesicle formation and function. Front Immunol. 2014;5:442.
68. Zhang Y, Tan J, Miao Y, Zhang Q. The effect of extracellular vesicles on the regulation of mitochondria under hypoxia. Cell Death & Disease. 2021;12(4):358.
69. Park JH, Hayakawa K. Extracellular Mitochondria Signals in CNS Disorders. Front Cell Dev Biol. 2021;9(248):642853.
70. Liu D, Gao Y, Liu J, Huang Y, Yin J, Feng Y, et al. Intercellular mitochondrial transfer as a means of tissue revitalization. Signal Transduct Target Ther. 2021;6(1):65.
71. Rutkai I, Merdzo I, Wunnava SV, Curtin GT, Katakam PV, Busija DW. Cerebrovascular function and mitochondrial bioenergetics after ischemia-reperfusion in male rats. J Cereb Blood Flow Metab. 2019;39(6):1056-68.
72. Ikeda G, Santoso MR, Tada Y, Li AM, Vaskova E, Jung J-H, et al. Mitochondria-Rich Extracellular Vesicles From Autologous Stem Cell–Derived Cardiomyocytes Restore Energetics of Ischemic Myocardium. Journal of the American College of Cardiology. 2021;77(8):1073-88.
73. Spees JL, Olson SD, Whitney MJ, Prockop DJ. Mitochondrial transfer between cells can rescue aerobic respiration. Proceedings of the National Academy of Sciences. 2006;103(5):1283-8.
74. Islam MN, Das SR, Emin MT, Wei M, Sun L, Westphalen K, et al. Mitochondrial transfer from bone-marrow–derived stromal cells to pulmonary alveoli protects against acute lung injury. Nature Medicine. 2012;18(5):759-65.
75. Hayakawa K, Esposito E, Wang X, Terasaki Y, Liu Y, Xing C, et al. Transfer of mitochondria from astrocytes to neurons after stroke. Nature. 2016;535(7613):551-5.
76. Sinha P, Islam MN, Bhattacharya S, Bhattacharya J. Intercellular mitochondrial transfer: bioenergetic crosstalk between cells. Current Opinion in Genetics & Development. 2016;38:97-101.
77. Gao L, Zhang Z, Lu J, Pei G. Mitochondria Are Dynamically Transferring Between Human Neural Cells and Alexander Disease-Associated GFAP Mutations Impair the Astrocytic Transfer. Front Cell Neurosci. 2019;13(316):316.
78. Guescini M, Genedani S, Stocchi V, Agnati LF. Astrocytes and Glioblastoma cells release exosomes carrying mtDNA. Journal of Neural Transmission. 2009;117(1):1.
79. Xiao B, Deng X, Zhou W, Tan EK. Flow Cytometry-Based Assessment of Mitophagy Using MitoTracker. Front Cell Neurosci. 2016;10(76):76.
80. Chazotte B. Labeling mitochondria with MitoTracker dyes. Cold Spring Harb Protoc. 2011;2011(8):990-2.
81. Mulcahy LA, Pink RC, Carter DR. Routes and mechanisms of extracellular vesicle uptake. J Extracell Vesicles. 2014;3(2001-3078).
82. Costa Verdera H, Gitz-Francois JJ, Schiffelers RM, Vader P. Cellular uptake of extracellular vesicles is mediated by clathrin-independent endocytosis and macropinocytosis. J Control Release. 2017;266:100-8.
83. Cronqvist T, Erlandsson L, Tannetta D, Hansson SR. Placental syncytiotrophoblast extracellular vesicles enter primary endothelial cells through clathrin-mediated endocytosis. Placenta. 2020;100:133-41.

84. Mohning MP, Thomas SM, Barthel L, Mould KJ, McCubbrey AL, Frasch SC, et al. Phagocytosis of microparticles by alveolar macrophages during acute lung injury requires MerTK. Am J Physiol Lung Cell Mol Physiol. 2018;314(1):L69-l82.
85. van Niel G, D'Angelo G, Raposo G. Shedding light on the cell biology of extracellular vesicles. Nat Rev Mol Cell Biol. 2018;19(4):213-28.
86. Parolini I, Federici C, Raggi C, Lugini L, Palleschi S, De Milito A, et al. Microenvironmental pH is a key factor for exosome traffic in tumor cells. J Biol Chem. 2009;284(49):34211-22.
87. Montecalvo A, Larregina AT, Shufesky WJ, Stolz DB, Sullivan ML, Karlsson JM, et al. Mechanism of transfer of functional microRNAs between mouse dendritic cells via exosomes. Blood. 2012;119(3):756-66.
88. Cronqvist T, Tannetta D, Mörgelin M, Belting M, Sargent I, Familari M, et al. Syncytiotrophoblast derived extracellular vesicles transfer functional placental miRNAs to primary human endothelial cells. Scientific Reports. 2017;7(1):4558.
89. Santos MF, Rappa G, Karbanová J, Kurth T, Corbeil D, Lorico A. VAMP-associated protein-A and oxysterol-binding protein-related protein 3 promote the entry of late endosomes into the nucleoplasmic reticulum. J Biol Chem. 2018;293(36):13834-48.
90. Petty RD, Sutherland LA, Hunter EM, Cree IA. Comparison of MTT and ATP-based assays for the measurement of viable cell number. J Biolumin Chemilumin. 1995;10(1):29-34.
91. Guo Y, Chi X, Wang Y, Heng BC, Wei Y, Zhang X, et al. Mitochondria transfer enhances proliferation, migration, and osteogenic differentiation of bone marrow mesenchymal stem cell and promotes bone defect healing. Stem Cell Res Ther. 2020;11(1):245.
92. Zhang J, Tan Z, Tran ND. Chemical hypoxia-ischemia induces apoptosis in cerebromicrovascular endothelial cells. Brain Res. 2000;877(2):134-40.
93. Andjelkovic AV, Xiang J, Stamatovic SM, Hua Y, Xi G, Wang MM, et al. Endothelial Targets in Stroke. Arteriosclerosis, Thrombosis, and Vascular Biology. 2019;39(11):2240-7.
94. Yang DI, Lin TN, Yin KJ, Hu CJ, Chen SD, Xu J, et al. Cerebral Endothelial Cell Reaction to Ischemic Insults. In: Lajtha A, Chan PH, editors. Handbook of Neurochemistry and Molecular Neurobiology: Acute Ischemic Injury and Repair in the Nervous System. Boston, MA: Springer US; 2007. p. 165-83.
95. Keep R.F. AAV, Stamatovic S.M., Shakui P., Ennis S.R. Ischemia-induced endothelial cell dysfunction. Intracranial Pressure and Brain Monitoring XII. 2005;95.
96. Park H-H, Han M-H, Choi H, Lee YJ, Kim JM, Cheong JH, et al. Mitochondria damaged by Oxygen Glucose Deprivation can be Restored through Activation of the PI3K/Akt Pathway and Inhibition of Calcium Influx by Amlodipine Camsylate. Scientific Reports. 2019;9(1):15717.
97. Liao L-X, Zhao M-B, Dong X, Jiang Y, Zeng K-W, Tu P-F. TDB protects vascular endothelial cells against oxygen-glucose deprivation/reperfusion-induced injury by targeting miR-34a to increase Bcl-2 expression. Scientific Reports. 2016;6(1):37959.
98. Kong LY, Liang MY, Liu JP, Lai P, Ye JS, Zhang ZX, et al. Mesenchymal Stem Cell-derived Exosomes Rescue Oxygen-Glucose Deprivation-induced Injury in Endothelial Cells. Curr Neurovasc Res. 2020;17(2):155-63.
99. Arslan F, Lai RC, Smeets MB, Akeroyd L, Choo A, Aguor ENE, et al. Mesenchymal stem cell-derived exosomes increase ATP levels, decrease oxidative stress and activate PI3K/Akt pathway to enhance myocardial viability and prevent adverse remodeling after myocardial ischemia/reperfusion injury. Stem Cell Research. 2013;10(3):301-12.

100. Pasquale D'Acunzo oP-G, Yohan Kim, Tal Hargash, Chelsea Miller, Melissa J. Alldred, Hediye Erdjument-Bromage, Sai C. Penikalapati, Monika Pawlik, Mitsuo Saito, Mariko Saito, Stephen D. Ginsberg, Thomas A. Neubert, Chris N. Goulbourne, Efrat Levy. Mitovesicles are a novel population of extracellular vesicles of mitochondrial origin altered in Down syndrome. Scientific Reports. 2021;7:eabe5085

101. Yetkin-Arik B, Vogels IMC, Nowak-Sliwinska P, Weiss A, Houtkooper RH, Van Noorden CJF, et al. The role of glycolysis and mitochondrial respiration in the formation and functioning of endothelial tip cells during angiogenesis. Scientific Reports. 2019;9(1):12608.

102. Smolina N, Bruton J, Kostareva A, Sejersen T. Assaying Mitochondrial Respiration as an Indicator of Cellular Metabolism and Fitness. Methods Mol Biol. 2017;1601:79-87.

103. Rose S, Frye RE, Slattery J, Wynne R, Tippett M, Pavliv O, et al. Oxidative stress induces mitochondrial dysfunction in a subset of autism lymphoblastoid cell lines in a well-matched case control cohort. PLoS One. 2014;9(1):e85436.

104. Wang Z, Guan D, Wang S, Chai LYA, Xu S, Lam KP. Glycolysis and Oxidative Phosphorylation Play Critical Roles in Natural Killer Cell Receptor-Mediated Natural Killer Cell Functions. Front Immunol. 2020;11(202):202.

105. GM C. The Mechanism of Oxidative Phosphorylation. The Cell: A Molecular Approach. 2. Sunderland (MA): Sinauer Associates; 2000.

106. King MP, Attardi G. Injection of mitochondria into human cells leads to a rapid replacement of the endogenous mitochondrial DNA. Cell. 1988;52(6):811-9.

107. Kadry H, Noorani B, Cucullo L. A blood–brain barrier overview on structure, function, impairment, and biomarkers of integrity. Fluids and Barriers of the CNS. 2020;17(1):69.

108. Li D, Duncan RF. Transient acquired thermotolerance in Drosophila, correlated with rapid degradation of Hsp70 during recovery. Eur J Biochem. 1995;231(2):454-65.

109. Zimmermann M, Traxler D, Simader E, Bekos C, Dieplinger B, Lainscak M, et al. In vitro Stability of Heat Shock Protein 27 in Serum and Plasma Under Different Pre-analytical Conditions: Implications for Large-Scale Clinical Studies. Ann Lab Med. 2016;36(4):353-7.

110. Miyata K, Oba M, Nakanishi M, Fukushima S, Yamasaki Y, Koyama H, et al. Polyplexes from Poly(aspartamide) Bearing 1,2-Diaminoethane Side Chains Induce pH-Selective, Endosomal Membrane Destabilization with Amplified Transfection and Negligible Cytotoxicity. Journal of the American Chemical Society. 2008;130(48):16287-94.

111. Haney MJ, Klyachko NL, Zhao Y, Gupta R, Plotnikova EG, He Z, et al. Exosomes as drug delivery vehicles for Parkinson's disease therapy. J Control Release. 2015;207:18-30.

112. Ramasubramanian L, Kumar P, Wang A. Engineering Extracellular Vesicles as Nanotherapeutics for Regenerative Medicine. Biomolecules. 2019;10(1):48.

113. Yuan D, Zhao Y, Banks WA, Bullock KM, Haney M, Batrakova E, et al. Macrophage exosomes as natural nanocarriers for protein delivery to inflamed brain. Biomaterials. 2017;142:1-12.

114. Zhang S, Hu Y, Huang Y, Xu H, Wu G, Dai H. Heat shock protein 27 promotes cell proliferation through activator protein-1 in lung cancer. Oncol Lett. 2015;9(6):2572-6.

115. Park A-M, Tsunoda I, Yoshie O. Heat shock protein 27 promotes cell cycle progression by down-regulating E2F transcription factor 4 and retinoblastoma family protein p130. J Biol Chem. 2018;293(41):15815-26.

116. Stetler RA, Gao Y, Signore AP, Cao G, Chen J. HSP27: mechanisms of cellular protection against neuronal injury. Curr Mol Med. 2009;9(7):863-72.

117. Venugopal A, Sundaramoorthy K, Vellingiri B. Therapeutic potential of Hsp27 in neurological diseases. Egyptian Journal of Medical Human Genetics. 2019;20(1):21.
118. Reddy VS, Madala SK, Trinath J, Reddy GB. Extracellular small heat shock proteins: exosomal biogenesis and function. Cell Stress Chaperones. 2018;23(3):441-54.
119. Wyciszkiewicz A, Kalinowska-Łyszczarz A, Nowakowski B, Kaźmierczak K, Osztynowicz K, Michalak S. Expression of small heat shock proteins in exosomes from patients with gynecologic cancers. Scientific Reports. 2019;9(1):9817.
120. Chanteloup G, Cordonnier M, Isambert N, Bertaut A, Marcion G, Garrido C, et al. Membrane-bound exosomal HSP70 as a biomarker for detection and monitoring of malignant solid tumours: a pilot study. Pilot and Feasibility Studies. 2020;6(1):35.
121. Takeuchi T, Suzuki M, Fujikake N, Popiel HA, Kikuchi H, Futaki S, et al. Intercellular chaperone transmission via exosomes contributes to maintenance of protein homeostasis at the organismal level. Proceedings of the National Academy of Sciences. 2015;112(19):E2497-E506.